A Spatial Multi-Omic Framework Identifies Gliomas Permissive to TIL Expansion

Authors:

Kelly M. Hotchkiss[1+],Kenan Zhang[1+], Anna M. Corcoran[1], Elizabeth Owens[1], Pamela Noldner[3], Chelsea Railton[1], Kyra Van Batavia[4], Ying Zhou[3], Jodie Jepson[5], Kirit Singh[1], Roger McLendon[1], Kristen Batich[1,2], Anoop P. Patel[1], Katayoun Ayasoufi[1], Michael C. Brown[1], Evan Calabrese[6], Jichun Xie[5,7,] Jose Conejo-Garcia[8], Beth H. Shaz[2,3], John W. Hickey[4,7], Mustafa Khasraw[1,5,8*]

Affiliations:

1 The Preston Robert Tisch Brain Tumor Center, Duke University; Durham, NC, US.
2 Department of Pathology, Duke University; Durham NC, US.
3 The Marcus Center for Cellular Cures, Duke University; Durham, NC, US.
4 Department of Biomedical Engineering Duke University; Durham, NC, US.
5 Computational Biology and Bioinformatics Program, Duke University; Durham, NC, US.
6 Department of Radiology, Duke University; Durham, NC, US.
7 Department of Biostatistics and Bioinformatics, Duke University; Durham, NC, US.
8 Department of Integrative Immunobiology, Duke University; Durham, NC, US.

[+]These authors contributed equally to the manuscript.

***Corresponding Author:**
Mustafa Khasraw, MD
The Preston Robert Tisch Brain Tumor Center
Duke University | Box 3624
Durham, NC 27710, USA
T +1 919.684.6173 | F +1 919.681.1697
E-mail: mustafa.khasraw@duke.edu

Keywords:
Glioblastoma, Astrocytoma, Tumor-Infiltrating Lymphocytes, Immunotherapy, TCR Profiling, Spatial Transcriptomics, Multiplex Proteomics, Single-Cell RNA Sequencing, Tumor Microenvironment, TIL Expansion

Article Type:
Research Article

Word Count:
3413

Figures & Tables:
Six Figures

Supplementary Information:
Available upon request.

Abstract

Tumor-infiltrating lymphocyte (TIL) therapy, recently approved by the FDA for melanoma, is an emerging modality for cell-based immunotherapy. However, its application in immunologically “cold” tumors such as glioblastoma remains limited due to sparse T cell infiltration, antigenic heterogeneity, and a suppressive tumor microenvironment. To identify genomic and spatial determinants of TIL expandability, we performed integrated, multimodal profiling of high-grade gliomas using spectral flow cytometry, TCR sequencing, single-cell RNA-seq, Xenium *in situ* transcriptomics, and CODEX spatial proteomics.

Comparative analysis of TIL-generating (TIL^+) versus non-generating (TIL^-) tumors revealed that *IL7R* expression, structured perivascular immune clustering, and tumor-intrinsic metabolic programs such as *ACSS3* were associated with successful TIL expansion. In contrast, TIL^- tumors were enriched for neuronal lineage signatures, immunosuppressive transcripts including *TOX* and *FERMT1*, and tumor-connected macrophages.

This study defines spatial and molecular correlates of TIL manufacturing success and establishes a genomics-enabled selection platform for adoptive T cell therapy. The profiling approach is now being prospectively implemented in the GIANT clinical trial (NCT06816927), supporting its translational relevance and scalability across glioblastoma and other immune-excluded cancers.

Tumor-infiltrating lymphocytes (TIL) therapy has shown efficacy in immune checkpoint inhibitor resistant melanoma[1,2]. The diverse tumor-specific targets of TIL make it an attractive therapy for heterogeneous tumors and resistance is less likely compared with cell therapies that have one or few targets[3]. In February 2024, the FDA approved lifileucel as the first TIL therapy to treat cancer confirming the future use of TILs in mainstream practice. However, the development of TIL therapy in immunologically “cold” tumors like high-grade gliomas is hampered by variability in TIL expansion, functional exhaustion of T cells, systemic and local immunosuppression, and tumor heterogeneity.

Prior studies highlight the role of T cell spatial heterogeneity and repertoire diversity in influencing TIL expansion potential[4]. Additionally, tumor-reactive TIL enrichment at baseline and clonotype dynamics have been identified as key determinants of therapeutic response, particularly in melanoma[5]. Integrated, multimodal characterization is emerging as a powerful approach for a holistic understanding of complex tumor microenvironments (TME) likely to drive future therapeutic precision approaches. Spatial omic technologies including genome, transcriptome, and proteome information retain spatial relationships to provide multidimensional, systems-level understanding of tumor biology[6-8]. Importantly, spatial approaches not only reveal the presence or absence of mutations, transcript abundance, and cell population compositions, but also offer insights into how spatial organization of cells and their coordinated cell-cell interactions drive differential responses to cancer treatment[9-14]. This may help characterize distinct immune multicellular environments across larger tissues[15], identify networks of important cell-cell interactions, analyze how they change in different spatial niches[12], track spatial and temporal tumor dynamics[11], and identify potential prognostic and predictive molecular signatures[10].

Despite using an optimized TIL expansion protocol, not all high-grade gliomas in our cohort successfully generated TILs. To investigate this variability, we performed an integrated multimodal analysis of cellular composition, TIL profiles, and molecular features. We conducted spectral flow cytometry on eighteen TIL products from eleven patients. We then focused on in-depth multi-omic comparisons of four tumors that generated yielding $\geq 10^8$ viable TILs and four non-generating tumors, all cultured under identical IL-2–based conditions. Expanded TILs were characterized via spectral flow cytometry and TCR sequencing to assess immune subsets, activation states, and clonality. Matched tumor tissues underwent single-cell RNA sequencing (scRNA-seq), *in situ* spatial transcriptomics (Xenium) with a custom glioma–immune gene panel and multiplexed spatial proteomics (CODEX) to evaluate immune infiltration and spatial architecture. Comparative TCR-seq and immunophenotyping revealed key differences in immune composition and clonal expansion. This systems-level analysis identifies features linked to successful TIL expansion, informing strategies to improve TIL manufacturing and immunotherapy efficacy in high-grade gliomas.

Results

Optimized IL-2–mediated TIL expansion protocol expands conventional CD4+ and CD8+ TILs

We attempted TIL expansion from glioblastoma and anaplastic astrocytoma tumors resected during surgery using an IL-2–based protocol (Fig. 1A). Final TIL yield depends on both pre-Rapid Expansion Protocol (pre-REP) numbers and Rapid Expansion Protocol (REP) fold expansion, both highly variable. We defined a minimum preREP threshold of 10^6 TILs per 0.5g tumor to initiate REP, and a successful expansion as $\geq 10^8$ final TILs, sufficient for downstream analysis and potential therapeutic use. This threshold reflects prior studies showing that effective TIL therapy requires robust *ex vivo* expansion while preserving cell viability and function.

Of eighteen expanded TIL products, eleven were $CD4^+$ dominant, three were $CD8^+$ dominant, three were evenly split, and one was enriched for NK T cells (Supplementary Fig. 1). Four samples from individual patients met the $\geq 10^8$ TIL yield and were selected for in-depth analysis. All showed significant expansion from preREP to REP (100–1,000-fold increase, Fig. 1B), meeting criteria for successful TIL expansion. Expanded TILs consisted mainly of $CD4^+$ and $CD8^+$ T cells (Fig. 1C). In two patients analyzed across both phases, cell composition remained stable (Supplementary Fig. 1B–C). Most $CD4^+$ and $CD8^+$ TILs exhibited an effector memory phenotype ($CD45RA^-CCR7^-$; Fig. 1C, 1E).

$CD4^+$ T cells included activated subsets: 30% $CD69^+$ (early) and 25% $CD25^+$ (late; Fig. 1F). $CD8^+$ T cells had 20% $CD69^+$, 35% $CD25^+$, and 30% HLA-DR^+, consistent with cytotoxic function. Although $CD8^+$ percentages were low in some samples, >80% expressed cytolytic markers CD95 and NKG2D, indicating strong killing potential. We also assessed suppressive and exhausted populations. Regulatory T cells ($CD4^+CD25^+Foxp3^+$) were <10% of $CD4^+$ T cells, and $CTLA4^+$ suppressive $CD4^+$ cells were <20%. Thus, high $CD4^+$ content did not reflect a high regulatory phenotype. Exhausted $CD4^+$ and $CD8^+$ T cells ($PD1^+TIGIT^+TIM3^+$) were present at low levels and lacked LAG3, suggesting a potentially non-terminally exhausted state (Fig. 1G).

To assess clonal overlap, we performed TCRseq on TIL products and matched tumor tissues. Donut plots showed limited clonal overlap (Fig. 1H). Although γδ TCRs were rare relative to αβ TCRs, their detection in TIL^+ products confirmed successful expansion (Fig. 1I), consistent with flow cytometry (Fig. 1C, Supplementary Fig. 1D). TCR metrics showed higher D50 and Diversity Index in γδ vs. αβ T cells, indicating a broader TCR repertoire and less clonal dominance in γδ T cells—suggesting a more diverse and potentially adaptable immune response.

Successful TIL expansion associated with baseline clonal frequency, intratumoral inflammation, and lower Treg signatures

To compare clonal distribution, we performed TCRseq on tumor tissues from both TIL^+ and TIL^- samples, along with non-malignant brain tissues from epilepsy surgery as controls (data not shown due to insufficient yield). While overall clonality did not differ significantly between TIL^+ and TIL^- tumors, TIL^+ samples showed

higher total and unique CDR3 reads (Supplementary Fig. 2), indicating greater T cell abundance or a more diverse TCR repertoire. Parallel library construction in non-malignant tissues yielded insufficient material, consistent with low lymphocyte infiltration. TIL^+ tumors also showed a trend toward a lower D50 index—meaning fewer T cell clones accounted for half of the total TCR repertoire—suggesting more selective clonal expansion, though the difference was not statistically significant. T cell receptor beta (TRB) clone distributions, representing the diversity and frequency of T cells based on their beta chain sequences, were ranked by frequency in TIL^+ and TIL^- tumors (Fig. 2A–B). In three TIL^+ cases with matched TIL product TCRseq, high-frequency clones in tumor were also detected in expanded TILs, suggesting clonal expansion during culture (Fig. 2A). Using a regulatory T cell (Treg) gene expression signature (Supplementary Table 2: FOXP3, IKZF2, IL10, LAG3, TGFB1, IL2RA, STAT5A), we performed immunophenotyping by next generation sequencing. TIL^+ tumors showed significantly lower Treg signature expression than TIL^- tumors (p=0.029, Mann–Whitney U test), suggesting a more immune-permissive TME (Fig. 2C). Additionally, Th1 and pro-inflammatory gene signatures were enriched in TIL^+ tumors, further highlighting immune landscape differences between TIL^+ and TIL^- tumors.

Clinical and MRI imaging features of TIL+ vs. TIL− tumors

The eight patients with high-grade gliomas ranged from 28 to 79 years old (Fig. 3), with a mix of newly diagnosed and recurrent tumors across various anatomical locations (frontal, temporal, parietal) (Supplementary Table 6). All TIL+ tumors were Isocitrate Dehydrogenase (IDH) wild type glioblastoma whereas TIL- tumors consisted of two IDH wild type glioblastoma and two IDH-mutated anaplastic astrocytoma. MRI features (Fig. 3) were heterogenous across both groups without any clear differences in enhancement pattern or non-enhancing peritumoral signal abnormality. Due to the small sample size, these findings should be interpreted with caution and require validation in larger cohorts.

Distinct immune and cellular landscapes define TIL+ and TIL− high-grade gliomas

To assess TME differences between TIL^+ and TIL^- tumors, we performed scRNA-seq on FFPE tissue. TIL^+ tumors were enriched in tumor-associated macrophages (TAMs), $CD8^+$ T cells, and mesenchymal-like gene signatures, while TIL^- tumors had higher levels of oligodendrocyte precursor cells (OPCs), astrocytes, and neuronal lineage markers, features of an immune-excluded phenotype (Fig. 4). Proportional analysis confirmed significantly more OPC-like tumor cells in TIL^- tumors (p=0.03) and a trend toward increased glial and neuronal cells.

Differential gene expression (using adjusted p-values) revealed genes upregulated in TIL^+ tumors (*ACSS3, IL7R, FOXD3, EHF, ELOVL2, IBSP*), suggesting a TME favorable for immune infiltration and TIL expansion (Fig. 4C). IL7R, a key regulator of T cell survival and proliferation—was among the top differentially expressed genes, supporting its role in cytokine-driven activation and TIL expansion. IL7R was most highly expressed in $CD4^+$ and $CD8^+$ T cells in TIL^+ tumors but also present at lower levels in non-lymphoid cells (AC-, OPC-, MES-like, and astrocytic tumor cells). To clarify whether IL7R expression in T cells contributed to the TIL^+

phenotype, we performed EdgeR-based differential analysis on $CD4^+/CD8^+$ cells alone, confirming IL7R upregulation in TIL^+ tumors and linking it to T cell–intrinsic cytokine responsiveness and *ex vivo* expandability.

ACSS3, involved in mitochondrial acetate and propionate metabolism, was also significantly upregulated in TIL^+ tumors and remained a top differentially expressed gene in AC-like cells, suggesting a tumor-intrinsic metabolic state promoting immune-permissive phenotypes, rather than shifts in cellular composition. In contrast, genes upregulated in TIL^- tumors (*LTBP4, GSTM1, FERMT1, GRID2, BMP2, TOX, HES6*) suggested TIL expansion limitation through effects on immune infiltration or T cell dysfunction. These genes are linked to TGF-β signaling, oxidative stress resistance, immune evasion, and exhaustion, factors contributing to TIL persistence and function.

Though not statistically significant, in the Xenium data, TIL^+ tumors tended toward more lymphoid cells and pro-inflammatory TAMs, while TIL^- tumors had more tumor cells, OPCs, and immunosuppressive TAMs. Individual UMAPs showed distinct cellular profiles—greater immune infiltration and activation in TIL^+ tumors vs. immune-excluded features in TIL^- tumors (Supplementary Fig. 3). Despite trends in immune composition, TCR clonality, and gene expression, the small sample size (n=8) limited statistical power. Larger cohorts and multi-region sampling, from necrotic core to proliferative edge—are needed to validate these findings and assess clinical significance.

Tumor-connected TAMs: Product of phagocytosis or potential driver of immune exclusion?

We identified a TAM subcluster expressing markers of tumor stemness *(SOX2, NES, MBP*), neural lineage (*PTPRZ1, NCAM1*), and glial identity (*AQP4, MBP, GJA1*). While this profile suggests a distinct TAM phenotype, alternative explanations include phagocytosis of tumor material, reactive astrocytes expressing macrophage genes, or microglia that have engulfed tumor cells. Unlike droplet-based scRNA-seq, where such signals may result from doublets, our probe-based spatial transcriptomics' segmentation algorithm reduces artifact likelihood. Due to the unclear nature of these TAMs, we refer to them as tumor-connected TAMs (Fig. 4B, 5; Supplementary Fig. 3–4, 7). Though not statistically significant, they trended more abundant in TIL^- tumors, suggesting a possible link to immune exclusion and reduced T cell infiltration.

Spatial immune clustering associates with successful TIL expansion

Spatial *in situ* transcriptomics imaging (Xenium) and multiplexed proteomics (CODEX) revealed distinct immune architectures in TIL^+ vs. TIL^- tumors. In TIL^+ tumors, $CD8^+$ and $CD4^+$ T cells formed structured clusters near vasculature, suggesting spatial immune surveillance and tumor–immune interaction (Fig. 5). In contrast, TIL^- tumors showed a diffuse, disorganized immune landscape with minimal T cell infiltration, indicative of an immune-excluded phenotype (Fig. 5). CODEX imaging confirmed perivascular immune aggregation in TIL^+ tumors, absent in TIL^- samples (Fig. 5, 6C–D). Quantitative spatial analysis linked immune clustering in TIL^+ tumors to increased $CD163^+$ macrophages and higher $CD8^+$ T cell density, suggesting a coordinated immune response within the glioma microvasculature.

Discussion

High-grade gliomas, particularly glioblastoma, remain a major clinical challenge due to their immunosuppressive microenvironment and limited treatment options. As a prototypical “cold” tumor, glioblastoma raises critical questions about the feasibility of TIL therapy in overcoming immune barriers. Despite low baseline T cell infiltration, we optimized TIL expansion protocols and showed that TILs enriched in $CD8^+$, conventional $CD4^+$, and γδ T cells, with minimal regulatory T cells, can be reliably expanded from resected high-grade glioma using a modified IL-2 preREP followed by standard REP (Fig. 1 and supplementary Fig 1). However, not all tumors support expansion, underscoring the need to understand influencing factors. Molecular profiling revealed distinct immune landscapes in TIL^+ vs. TIL^- tumors. TIL^+ tumors showed pro-inflammatory clustering and immune activation, while TIL^- tumors were enriched in neuronal-like features and suppressive markers. Mesenchymal-like programs correlated with immune infiltration in TIL^+ tumors, whereas OPC and astrocytic signatures predominated in TIL^- tumors. These findings suggest TIL expansion depends not only on lymphocyte presence but also on the functional and cellular state of the TME.

IL7R gene was upregulated in tumors with successful TIL expansion, suggesting that responsiveness to homeostatic cytokine signaling[16] (e.g., IL-7) may support the maintenance and proliferative potential of T cells during *ex vivo* expansion. While IL-2 has traditionally been used to support TIL growth, its use can promote terminal differentiation and T cell exhaustion, ultimately compromising T cell persistence and anti-tumor functionality following infusion[17]. IL-7 also promotes a memory phenotype[18], enhances Chimeric Antigen Receptor (CAR) T-Cell Therapy infiltration into solid tumors[19], and as we have shown recently in murine glioma models[20], increases CD8+ T cell numbers. Taken together, these findings highlight the need for future studies directly comparing IL-7– and IL-2–based TIL expansion protocols to determine whether IL-7 enhances effector function and reduces inhibitory signaling. Further investigation is warranted to validate *IL7R* as a predictive biomarker and to assess the potential of IL-7 as an alternative or adjunct to IL-2 in optimizing TIL expansion for therapeutic use.

In addition to well-established T cell-related genes, we identified upregulation of *ACSS3* and *GSTM1* in the TIL^+ tumors, genes that may influence tumor and immune metabolism. Although speculative, *ACSS3*, which mediates acetate metabolism[21], and supports lipid biosynthesis and metabolic flexibility in tumor cells, was upregulated in TIL^+ tumors, including within AC-like tumor cells. This suggests a tumor-intrinsic metabolic adaptation that may promote a microenvironment favorable to TIL survival or expansion. These findings raise the possibility that *ACSS3* could function both as a biomarker and a mediator of TIL-supportive states. Whether it directly facilitates immune infiltration or enhances tumor resilience under immune pressure remains to be tested. *GSTM1*, an enzyme involved in detoxification and oxidative stress response, catalyzes glutathione conjugation for cellular elimination[21]. Its upregulation in TIL− tumors suggests a role in tumor adaptation to oxidative stress, potentially contributing to immune suppression. However, direct evidence of its impact on

immune modulation in glioblastoma is lacking. Functional studies are needed to determine whether any of these genes plays an active role in shaping the tumor immune microenvironment or if its expression reflects broader metabolic reprogramming.

Pseudobulk RNA expression analysis using EdgeR on both Xenium and scRNA-seq data identified overlapping elevated expression of *TOX* and *FERMT1* in TIL$^-$ tumors. This is notable given that scRNA-seq includes >18,000 genes, while our Xenium panel only included a customized 480-gene panel. Although the differential expression analysis does not account for spatial context in the Xenium data, the results still highlight key features of immune-permissive TMEs in TIL$^+$ tumors (Fig. 4). Upregulation of *MOXD1* and *DUSP4* in the TIL$^+$ tumors suggests a microenvironment conducive to immune infiltration and TIL persistence. *MOXD1* is involved in the development of glioblastoma[22], but its functional role remains unclear and warrants further investigation. *DUSP4* activity affects cell migration[23], proliferation[24], extracellular matrix[23]. Together, upregulation of these genes in TIL+ tumors supports a niche in which TILs remain functionally active and capable of expansion.

FERMT1 was consistently upregulated in TIL$^-$ tumors across both scRNA-seq and Xenium pseudobulk DGE analyses, suggesting a role in promoting immune exclusion. *FERMT1* encodes kindlin-1, an integrin-activating protein highly expressed in epithelial tissues, originally linked to Kindler syndrome and implicated in various cancers[25,26]. *FERMT1* may help establish a physical and molecular barrier to T cell infiltration, supported by transcriptional signatures of increased tumor stemness; its suppression reduces stemness and promotes anti-tumor effects in glioma cells[27], indicating a more undifferentiated and immune-resistant TME in TIL$^-$ tumors. In contrast, TIL$^+$ tumors showed elevated *IL7R* expression, indicating a more immune-permissive environment where *IL7R*-driven homeostatic signaling may support T cell survival and expansion.

Xenium and multiparametric flow cytometry identified distinct TAM subsets in TIL$^-$ tumors. Immunosuppressive TAMs expressed CD68, CD163, *TGFB1, TREM2, and TMEM119*; pro-inflammatory TAMs expressed CXCL8, CXCR4, and CCL5. TIL$^+$ tumors showed increased immune recruitment (CXCL8, CCL2, CD163), while TIL$^-$ tumors expressed immunosuppressive markers (*TOX, SFRP2, LTBP4*) and neuronal genes (*NRXN1, OLIG2*), indicating tumor-driven immune evasion.

A TAM subcluster expressed tumor stemness genes (*SOX2, NES, MBP*), neural lineage markers (*PTPRZ1, NCAM1*), and glial markers (*AQP4, MBP, GJA1*), suggesting origins via phagocytosis, reprogramming, or mimicry. We designated these tumor-connected TAMs. H&E and Xenium analysis showed they localize to necrotic, edematous, or fibrotic regions, separated from viable tumor (Supplementary Fig. 7). This pattern was consistent across specimens and histologies. Though not statistically significant, they appeared to be more abundant in TIL$^-$ tumors (Fig. 4B), potentially contributing to immune exclusion. Their role—passive or active—requires further study via lineage tracing and functional assays.

Beyond molecular profiling, spatial immune architecture distinguished TIL$^+$ tumors, where lymphoid cells formed structured perivascular aggregates (Fig. 5–6), suggesting vascular niches support antigen presentation and T cell activation, consistent with single-cell studies showing endothelial and mural cell specialization in coordinating immune infiltration in glioblastoma[28]. In contrast, immune cells in TIL$^-$ tumors were sparse and disorganized, with minimal intratumoral penetration (Fig. 5–6). This study also confirms the well-documented intra- and interpatient heterogeneity of glioblastoma[29]. Like findings in other studies[30,31], immunosuppressive myeloid-tumor interactions within specific cell niches may not only inhibit anti-tumor responses but also prevent successful TIL generation. Tertiary lymphoid structures (TLS) have been described in gliomas[32,33], but the immune aggregates observed here (Fig. 5) do not meet the criteria for mature TLS in cancers[34], necessitating further characterization. Emerging studies also highlight the prognostic and predictive value of spatial data in gliomas[35,36].

A persistent limitation across most spatial transcriptomic and single-cell RNA sequencing studies—including those published in high-impact journals—is their reliance on retrospectively banked biospecimens. While these studies have yielded important insights, they are inherently vulnerable to immortal time bias, as biospecimens are typically collected post hoc and outside defined clinical timelines. This bias constrains the ability to resolve temporal relationships between biological features and clinical outcomes, limiting the translational utility of candidate biomarkers.

To overcome these limitations, we prospectively integrated multi-platform immune and spatial profiling—including flow cytometry, TCRseq, scRNA-seq, Xenium *in situ* transcriptomics, and CODEX multiplexed spatial proteomics, within the Glioblastoma Immunotherapy Advancement with Nivolumab and Relatlimab (GIANT) trial (NCT06816927). This clinical trial enables real-time, pre-treatment tissue acquisition with longitudinal follow-up and uniformly annotated clinical metadata, establishing a rigorous framework for biomarker discovery and validation.

Despite the modest cohort size (n=8; 4 TIL$^+$, 4 TIL$^-$), convergence across orthogonal technologies supports the robustness of the findings. We observed consistent immunologic features across flow cytometry, TCR sequencing, single-cell and spatial transcriptomics, and multiplexed proteomics, enabling cross-platform validation. Where possible, we quantified overlap—for example, by calculating the percentage of TCRs shared between tumor tissues and expanded TIL products. Statistical analyses, including EdgeR for differential expression and Mann–Whitney U tests for group comparisons, were applied to maximize interpretability and analytical rigor.

This study identifies cellular and molecular features associated with the successful expansion of TILs from primary glioblastomas. I*L7R* expression and structured perivascular immune clustering were consistently enriched in TIL$^+$ tumors, suggesting that local immune architecture may support effective TIL priming. Notably, tumor-intrinsic expression of *ACSS3*, a regulator of acetate metabolism—was upregulated in astrocyte-like malignant cells in TIL$^+$ samples, suggesting a metabolic phenotype conducive to immune engagement. In

contrast, TIL⁻ tumors were enriched for tumor-connected, immunosuppressive TAMs, consistent with a spatially immune-excluded phenotype.

These findings align with broader features of immune-cold tumors, including glioblastoma, pancreatic, prostate, and hormone receptor–positive breast cancers, where low antigenicity, MHC class I downregulation, and antigenic heterogeneity limit T cell engagement. Antigen specificity remains a major determinant of TIL efficacy, and approaches such as neoantigen-enriched TIL products, TCR-guided selection, or combination immunotherapies may improve outcomes in these settings. Our platform provides a mechanistic link between spatial immune context and antigen recognition, offering a path toward biomarker-driven patient stratification and personalized cell therapy manufacturing.

Importantly, this study should be interpreted as a discovery-stage, platform-development effort rather than a therapeutic efficacy evaluation. The integration of all profiling protocols within a prospective clinical trial framework addresses common limitations of retrospective datasets and establishes a foundation for future validation. Larger, multi-institutional cohorts with functional studies will be essential to confirm the predictive relevance of candidate biomarkers, including *IL7R*, spatial immune clustering, tumor-associated macrophage states, and tumor-intrinsic metabolic programs.

Together, these findings establish a spatially resolved, clinically integrated discovery platform to identify gliomas permissive to TIL therapy. The ability to couple real-time tissue acquisition with multimodal profiling and clinical annotation supports early decision-making on TIL manufacturing and informs the design of next-generation strategies, including neoantigen discovery pipelines and engineered TIL products. The approach is generalizable to other immune-resistant solid tumors, providing a translational framework to guide immunotherapy deployment in anatomically and immunologically challenging malignancies.

Acknowledgements:

General

The authors are grateful to all patients who consented to donate biospecimens for this study. We thank the team at the Duke Brain Tumor Biorepository for their assistance and co-ordination in tissue management and slide preparation. We would also like to acknowledge the assistance of the Molecular Genomics Core at the Duke Molecular Physiology Institute, Duke University School of Medicine, for the generation of data for the manuscript.

Funding

NIH Duke SPORE (P50 CA190991-08**)** DRP grant (MK and KMH)

Knox Martin Foundation (MK)

Barzun and Siebert Funds (MK)

Viral Oncology T32 (T32CA009111) (KMH)

Institutional Review Board (IRB)/ Ethics approval:

All human samples were collected on Duke IRB protocol number Pro00106078.

Author contributions

Conceptualization: KMH, PN, BS, JWH, MK

Methodology: KMH, KZ, AMC, EO, JWH, MK

TIL expansion: PN, YZ, BS

scRNAseq library preparation: CR, KMH

Xenium Slide preparation: Duke Brain Tumor Biorepository

Xenium raw data generation: The Molecular Genomics Core at the Duke Molecular Physiology Institute, Duke University

Neuroradiology: EC

Custom Xenium Panel Design: KMH, AMC, JCG, MCB, KA, MK

scRNA analysis: EO

spatial RNA Xenium data analyses: AMC, KZ, MK

Bulk RNA/ TCRseq: KZ, MK

Codex: JWH, KVB

Flow cytometry: KMH

H&E slides and images review: RM

Writing – original draft: KMH, EO, AMC, KZ, BS, KVB, JWH, MK

Writing – review & editing: all authors

Supervision: MK

Competing Interests

JCG reports honoraria from Alloy Therapeutics, patent licensing fees from Anixa Biosciences, intellectual property with Anixa Biosciences, Compass Therapeutics and Cellepus Therapeutics, and equity as a co-founder of Cellepus Therapeutics.

MK reports grants or contracts from BMS, AbbVie, BioNTech, CNS Pharmaceuticals, Daiichi Sankyo Inc., Immorna Therapeutics, Immvira Therapeutics, and Personalis, Inc.; received consulting fees from JAX lab for Genomic Research, George Clinical, Manarini Stemline, and Servier; received honoraria from GSK; and is on the scientific advisory boards of George Clinical, Siren Biotech., and a data safety monitoring boards for BPG Bio and The University of Pennsylvania Center for Cellular Immunotherapies.

Online Methods

Sample Preparation

The glioma samples were collected as per Duke Institutional Review Board approved protocol “Collection of Solid Tumor Specimens for Pre-clinical Development and Manufacturing of a Clinical Tumor Infiltrating Lymphocyte (TIL) Cell-therapy Product” Pro00106078 for the collection of the preclinical development samples. Patients were consented for biobanking of their tumor and blood specimens, sample acquisition and data collection.

TIL Expansion

Autologous TILs were produced in the process development lab at the Marcus Center for Cellular Cures at Duke University. TIL expansion was performed using a portion of the resected tumor that was distinct from the sample used for multimodality analyses, ensuring that immune profiling of the original tumor tissue remained unaffected by the *ex vivo* expansion process. Fresh tumors samples were weighted, cut to small fragments of 2-3mm^3 and placed into G-Rex flasks at 5-24 mg/cm^2 culture surface in preREP media containing PrimeXV T cell expansion media (FujiFilm), 5% human platelet lysate (hPL, Compass Biomedical), 4000 IU/ml IL-2 (Proleukin or BioTechne), Pen/Strep (Gibco) and expanded for 18-28 days. TILs were collected on harvest day, counted, cryopreserved in CryoStor CS10 (BioLife Solutions) and stored in N_2. For REP expansion, preREP TILs were thawed, washed and placed into a G-Rex flask at 1e6/ml*cm^2 in REP media (PrimeXV T cell expansion media, 3% hPL, 1000IU/ml IL-2) and activated by addition of CD3/CD28 nanoparticles (TransAct, Miltenyi Biotec). After 3 days, the activation was stopped by dilution with REP media to the fill mark of the G-Rex flask. Culture media was replaced when media lactate reached 15mM. REP TILs harvested on culture day 14 and cryopreserved in CS10.

In some cultures, additional immune-modulating antibodies were incorporated into the preREP phase to assess their impact on TIL expansion. These included atezolizumab (an anti–PD-L1 antibody), nivolumab and pembrolizumab (anti–PD-1 antibodies), and urelumab (an agonistic anti–4-1BB antibody). These agents were selected based on their known roles in enhancing T cell activation and survival by blocking inhibitory signals (PD-1/PD-L1 axis) or stimulating co-stimulatory pathways (4-1BB), and were added alongside IL-2 to test whether their inclusion could augment TIL yield or function.

Flow Cytometry

Cryopreserved cells were rapidly thawed in a 37C water bath and resuspended in RPMI media with 2% fetal bovine serum. Cells were then pelleted at 300xg for 5 minutes at 4C and resuspended to count by hemocytometer. One million cells per well were loaded into a round bottom 96 well plate for flow staining. Cells were first stained with LiveDead Blue Fixable viability dye (Invitrogen), then blocked with buffer containing anti-CD16/32 (Invitrogen) and mono-block (BioLegend). A master mix containing all surface antibodies (Supplementary Table 1) was prepared in brilliant violet stain buffer (Invitrogen) and added on top of blocking

buffer for 30 mins. Cells were then fixed and permeabilized using the eBioscience™ Foxp3 / Transcription Factor kit to allow for intracellular staining of FOXP3, CD69, CD137 and CTLA4. Spectral data was collected on the Cytek Aurora 5L and analyzed by FlowJo v10.

Sample Preparation for multimodality analyses

Formalin-fixed paraffin-embedded (FFPE) tissues were processed for single-cell and xenium profiling, followed by bulk TCRseq and CODEX multiplexed imaging.

Formalin-Fixed Paraffin-Embedded (FFPE)

5μm FFPE tissue sections are placed on a 10x Genomics Xenium slide. Tissue slides are deparaffinized and decrosslinked. Next, tissue is processed through Hybridization, Ligation & Amplification protocols. Prepared tissue slides are then loaded for imaging on the Xenium Analyzer for *in situ* analysis. Cyclical rounds of fluorescent probe hybridization, imaging, and removal generate optical patterns specific for each barcode, which are converted into a gene identity. Identified transcripts are then visualized using Xenium Explorer software. H&E staining was performed on the slides following Xenium analysis to allow for histopathological assessment.

FFPE with Custom Panel and Multimodal Segmentation

5um FFPE tissue sections are placed on a 10x Genomics Xenium slide and baked at 42C for 3hours. Once dried, tissue slides are stored in a desiccator to await processing. Xenium slides are then incubated at 60C for 2 hours and then deparaffinized and decrosslinked. Briefly, sections are deparaffinized via xylene immersion to solubilize the paraffin, ethanol to remove the solubilized paraffin and slowly hydrate the tissue, and then immersed in water to remove residual ethanol. Once hydrated, tissues slides are decrosslinked. Tissue slides are inserted into 10x Genomics Xenium slide cassettes. Decrosslinking buffer is then added to the well created by the cassette and incubated. After incubation, the buffer is removed, and the sample is washed. Tissue is then processed through Hybridization, Ligation & Amplification protocols. Briefly, a custom panel containing probes for 480 custom gene panel *(The gene list is available as a supplementary file)* enriched in genes relevant to glioma, neuronal and immune cells, is added to the tissue. The 480-gene panel was used to enable mapping of gene expression in the tissue architecture. Differential expression analyses highlighted immune-tumor dynamics in pro-inflammatory and immunosuppressive pathways. Each circularizable DNA probe contains two regions that hybridize to target RNA and a third region that encodes a gene-specific barcode. The two ends of the probes bind the target RNA and are ligated to generate a circular DNA probe. Following ligation, the circularized probe is amplified, producing multiple copies of the gene-specific barcode for each target. Tissue slides are then stained using the 10x Genomics Multimodal Cell Segmentation Kit. During Multimodal staining, antibodies used for cell segmentation bind their antigens in an overnight incubation, followed by post-incubation washes to remove excess antibodies. The cell segmentation stain is then enhanced by 10x Genomics proprietary reagents. The Multimodal Cell Segmentation kit stains for cell nuclei,

membranes, and cell interior that are inputs for the 10x Genomics automated morphology-based cell segmentation analysis pipeline. Prepared tissue slides are then loaded for imaging on the Xenium Analyzer for *in situ* analysis. Fluorescently-labeled oligos bind to the amplified DNA probes. Cyclical rounds of fluorescent probe hybridization, imaging, and removal generate optical patterns specific for each barcode, which are converted into a gene identity. Identified transcripts are then visualized using Xenium Explorer software.

Chromium Single Cell Gene Expression Flex (scFFPE-seq)

For each sample, 2x 25 µm FFPE curls were dissociated in accordance with 10x Genomics "Isolation of Cells from FFPE Tissue Sections for Chromium Fixed RNA Profiling protocol (User guide CG000632, Rev. B). Following cell isolation, samples underwent probe hybridization with one probe barcode per sample from the 10x Genomics Single Cell Fixed RNA Human Transcriptome Probe Kit. Approximately 151,050 cells per sample were pooled, washed, filtered, and loaded into 10x Genomics' Next Gem Chip Q targeting a recovery of 8,000 cells per probe barcode. Sequencing libraries were generated following 10x Genomics' User Guide CG000527 for Fixed RNA Profiling (Rev. E). The tumor samples from eight patients were used to generate two libraries following 10x Genomics' User Guide CG000527 for Fixed RNA Profiling (Rev. E). These libraries were sequenced on an Illumina NovaSeq platform, resulting in four FASTQ files per library. Individual samples in each library were demultiplexed by their incorporated barcodes using CellRanger's (v7.0.1) multi pipeline and the GRCh38-2020-A reference (10x Genomics). Following demultiplexing, sequencing data from each sample was obtained, enabling data analysis across both libraries. CellRanger's aggr pipeline was utilized to aggregate data from the same patients, treating data from different libraries as independent replicates to evaluate any biological variability and to provide more substantial cell counts.

Single-Cell RNA Sequencing (scRNA-seq)

CellRanger's pipelines corrected for empty droplets, cells with few transcripts, an important variable in quality control filtering. Cells were further filtered to ensure high quality reads, which including removing ambient RNA and potential doublets. Specifically, cells with greater than 10000 detected transcripts, greater than 7000 detected genes, a mitochondrial gene proportion exceeding 20%, a cell complexity below 80% (log10Gene/log10UMI), and a hemoglobin gene proportion above 2% were excluded before downstream analysis. The hemoglobin gene threshold of 2% was stringent since only a few cells across the eight samples exceeded this level, reflecting the solid tissue origin of the samples. Genes present in fewer than three cells per sample were also removed to eliminate low-abundance genes and correct potential misreads from the reference transcript. Although a threshold of 30 cells is commonly used, this was adjusted due to the low cell count of these samples, ranging from 539 to 1429 cells. Ribosomal gene proportions, another common parameter, were not applicable because CellRanger's reference transcriptome excludes ribosomal reads. Violin plots confirmed that filtering did not result in significant data loss, but this filtering ensures that downstream analysis will not be influenced by technical variations or losses.

After normalization and scaling, the data was batch-corrected and integrated using Seurat's integration pipeline. The IntegrateLayers function employs canonical correlation analysis (CCA), a method akin to principal

component analysis, to identify shared sources of variation between sample groups (TIL+ vs. TIL-). Jackstraw plots and clustree were used to determine the appropriate number of principal components and value of resolution, respectively, before running this analysis. This approach removes non-biological variation, accounts for confounding factors, and enables comparative analysis between groups. To ensure reproducibility, a random seed was set for Seurat's RunPCA, FindClusters, and RunUMAP.

Post-integration, clusters identified using Seurat's integration method were automatically annotated using the SingleR package (https://github.com/dviraran/SingleR?tab=readme-ov-file), referencing a single-cell RNA sequencing glioblastoma dataset from CELLxGENE (https://cellxgene.cziscience.com/collections/999f2a15-3d7e-440b-96ae-2c806799c08c). SingleR, a correlation-based method, matches the full transcriptome of query cells to reference cells rather than relying solely on marker gene expression. Annotation accuracy was assessed by identifying differentially expressed genes (DEGs) for each cluster using Seurat's FindMarkers function, comparing each cluster against the remaining cells. Tumor subtypes were validated based on prior literature[37], with AC-like clusters expressing GFAP, BCAN, SPARC, and DBI; MES-like clusters expressing HILPDA, CA9, ADM, and VIM; NPC-like clusters expressing DCX, DLX5, SOX4, DBN1, and RND3; and OPC-like clusters expressing NEU4, PTPRZ1, LIMA, VCAN, and OLIG1. Non-malignant clusters were further validated using marker genes from CellMarker2.0[38] and published literature[39,40]: astrocytes (GFAP, CLU, AQP4, S100B), CD4/CD8 T cells (CD3E, CD3D, CD3G, GMZA, SKAP1), endothelial cells (VWF, CLDN5, CLEC14A, CDH5), mural cells (CD248, PDGFRB, RGS5, FOXF2), neurons (SYT1, SNAP25, GABRA1, NRCAM), oligodendrocytes (MOG, MBP, OLIG1, OLIG2, CLDN1), OPCs (SOX10, PDGFRA, APOD, OLIG1, OLIG2), TAM-BDM (CD163, CD14, TGFBI, ITGA4, MARCO), TAM-MG (TMIGD3, APOC2, SCIN, P2RY12, NAV3), and monocytes (LYZ, AREG, CD163, CD68, MXD1).

Differential gene expression (DEG) analysis was conducted between TIL+ and TIL- groups using EdgeR, a Bioconductor software package for examining differential expression of replicated count data[41]. These methods were also applied to identify differentially expressed genes among cell types within each group.

Cell composition analysis was performed between the two groups to identify the proportion of each cell type in the TIL+ vs TIL- samples. The Mann-Whitney U test was used to determine whether the differences in cell composition between the sample groups were significant. Notably, the proportion of OPC-like tumor cells was significantly higher in TIL- samples compared to TIL+ samples. Violin plots were also made to illustrate sample variability in cell compositions.

Spatial Transcriptomics

For analysis of each Xenium sample, centroid (location), segmentation (cell boundaries), and the counts matrix data were extracted. Samples were loaded and filtered to keep cells with more than five features and more than ten counts, with 0.7% of cells removed on average. The *ComputeBanksy* (Prabhakar lab) function was used on all the samples with a lambda of 0.2 to create a spatially informed matrix. Both the regular expression and Banksy matrices were extracted along with cell location to create a Seurat object. The standard Seurat and Harmony pipeline (functions: *NormalizeData*, *FindVariableFeatures*, *ScaleData*, *RunPCA*, *FindNeighbors*, *FindClusters*, *RunUMAP*) (https://satijalab.org/seurat/articles/seurat5_integration) was used to integrate the

eight samples with the *IntegrateLayers* function (method=HarmonyIntegration), and all further analysis was based on the harmony clusters. This produced eight clusters, which were manually labeled as: Glial/Tumor cells (clusters 0,1, 3, 7, based on GFAP, MKI67, OLIG2, SOX2, EGFR, CDKN2A, OLIG1, and TP53), TAMs (clusters 2 and 4, based on CD68, CD163, CXCL8, ITGAX, and CCL5), Lymphoid (cluster 8, based on PTPRC, CD3E, CD4, and CD8A), Oligodendrocyte/OPC (cluster 5, based on MAG, MBP, and SOX10), and Endothelial (cluster 6, based on VWF, PDGFB, and CD34). These were then further clustered based on the Banksy matrix for those cells to get more specific cell types. The same Seurat pipeline was run on the Banksy matrix for each group of cells, and then FindAllMarkers was run on the Harmony matrix for annotation. First, clusters 2 and 4 were extracted and reclustered, producing three clusters which were labeled as “Tumor-Connected TAM" (SOX2, NES, and MBP), "Immunosuppressive TAM" (CD68, CD163, TGFB1, TREM2, and TMEM119), and "Pro-inflammatory TAM” (CXCL8, CXCR4, and CCL5) based on their differentially expressed marker genes calculated by FindAllMarkers.

Then, the same steps were followed for clusters 0, 1, 3, 5, and 7 to get more accurate tumor and normal brain clusters, generating a total of eight new clusters. These were labeled as OPC-like (OLIG1, PDGFRA, NLGN3, and LHFPL3), MES-like (CD44, ANXA1, SOD2, VIM, and DDIT3), NPC-like (DCX, SAOX11, SOX4, and ASCL1), AC-like (GFAP, AQP4, and HOPX), Proliferative-1 (PCNA, FOXM1, and OLIG1), Proliferative-2 (PCNA, GOXM1, CCNB2, SOX11, ASCL1, and DCX), Oligo/OPC (OLIG1 and SERINC5), and Neuronal cells (SLC17A7, NRXN1, SYNPR, and GAD1) respectively, based on their FindAllMarkers gene results. Original cluster labels were compared to these new labels, and non-tumor clusters retained the majority of the cells, improving the validity of the clustering. All these subclusters were mapped back onto the original Harmony UMAP and then plots were made by TIL type (TIL or no TIL) and by each sample.

Differential gene expression (DEG) analysis was conducted between TIL+ and TIL- groups using EdgeR[41]. These methods were also applied to identify differentially expressed genes among cell types within each group. Statistical testing using Mann-Whitney was performed to determine whether the differences in cell composition between the sample groups were significant, and no significant differences were found.

CODEX Multiplexed Imaging and Data

Array creation

Imaging data was collected from multiple brain samples from multiple donors on one slide. We included up to six tissues that were cut onto the same slide with a 4 µm section thickness and mounted onto Superfrost PLUS slides for further processing.

Antibody conjugation

Each antibody was conjugated to a unique oligonucleotide barcode using our previously established protocol[42], after which the tissues were stained with the antibody–oligonucleotide conjugates and we validated that the staining patterns matched the expected patterns already established for immunohistochemistry within positive control tissues of the intestine or tonsil. Otherwise, expected co-expression of markers in the case of staining of suspension cells was taken into account for validating separate cell type and phenotype antibodies. First,

antibody–oligonucleotide conjugates were tested in low-plex fluorescence assays and the signal-to-noise ratio was also evaluated at this step, then they were tested all together in a single CODEX multicycle. Antibody information can be found in Supplementary Table 1.

CODEX staining and imaging

The tissue arrays were stained with the validated panels of CODEX antibodies and imaged. Briefly, this entailed cyclic stripping, annealing, and imaging of fluorescently labeled oligonucleotides complementary to the oligonucleotide conjugated to the antibody as described[42]. Each slide underwent CODEX multiplexed imaging using Akoya Phenocycler Fusion machine; metadata from each CODEX run can be found in the supplementary files.

TCR Repertoire and Immunophenotyping Analyses

T cell receptor sequencing (TCRseq) was performed using iRepertoire's RepSeq+ technology to assess the diversity and clonality of immune repertoires. The diversity and clonality of tumor-infiltrating lymphocyte (TIL) populations were evaluated, with a specific focus on clonal expansions, particularly among CD8+ T cells in TIL+ tumors, to quantify tumor-reactive TCR frequencies. ImmunoSight, a targeted NGS assay of 150+ immunophenotype genes, alongside the RepSeq+ was performed to detect the immune response of the corresponding samples.

TCRseq

RNA was extracted from TIL samples using the PAXgene RNA Extraction Kit (PreAnalytix), and total RNA were extracted from FFPE samples using the Covaris truXTRAC FFPE total NA Plus Kit, and SPRIselect beads were used for RNA concentration to maximize input for amplification. 1600 ng of RNA per sample, along with replicates, was utilized for RepSeq+ TCR alpha, beta, delta, and gamma chain amplification. The RepSeq+ protocol facilitated simultaneous amplification of all four TCR chains under uniform conditions using primer pairs specific to V-D-J combinations, incorporating unique molecular identifiers (UMIs) during reverse transcription to minimize sequencing errors and PCR duplicates. Sequencing was performed on the Illumina NextSeq 1000 platform using a P1 600-cycle kit. Data analysis was conducted using the iRmap pipeline, which involved de-multiplexing sequence reads, mapping them to IMGT germline reference sequences, and extracting CDR3 regions. The final dataset was refined by collapsing identical CDR3 and UMI combinations to correct for sequencing errors. TCR repertoire diversity and clonality were evaluated by D50, Diversity index, and Shannon entropy. The D50 is the percentage of dominant and unique T cell clones that account for the cumulative 50% of the total CDR3s counted. The diversity index is 100 minus the area under the curve between the percentage of total reads and the percentage of unique CDR3s.

Immunophenotyping

A total of 5 µL of extracted RNA from both the TIL and FFPE samples was used for immunophenotyping. Library construction included cDNA purification via SPRIselect bead purification, followed by two rounds of

gene-specific amplification and adapter ligation to generate Illumina-compatible libraries. Immunophenotyping data were analyzed by aligning reads to a reference database of expected amplicons using bowtie2 with gene counts normalized across samples. Immune cell type and immune response scores were generated by Gene Set Variation Analysis (GSVA) and visualized by ComplexHeatmap. The gene signatures used are listed in Supplementary Table 2.

Data availability

Raw and processed data available on request.

Code availability

TCRseq data, processed scRNA data and Xenium expression matrix with coordinates are available on GitHub athttps://github.com/khasrawlab/TILproject.

All demographic, flow cytometry data are available in the manuscript. Metadata and the custom gene panel is available as supplementary files.

Codex and Xenium images are available on FigShare at https://figshare.com/s/5e47e57a6c1de924098e

Figures legends

Figure 1: Pre-Rapid Expansion Protocol (preREP) and Rapid Expansion Protocol (REP) Tumor-Infiltrating Lymphocyte (TIL) T-Cell Receptor (TCR) and Flow Cytometry Analysis. (A) Schematic diagram of TIL expansion. (B) Expansion of TILs from preREP to REP with TIL numbers significantly increasing from preREP to REP (paired t-test, $p = 0.020$). Flow analysis characterizing (C) overall cell types and memory T cell subsets in (D) CD4 and (E) CD8 cells in REP TIL product from patients 23-0257, 23-0227, 22-0189, and 23-0153. (F) Percentage of activated CD4 and CD8 cells expressing CD69, CD25, HLA-DR as well as cytolytic molecules CD95 and NKG2D. (G) Suppressive CD4+ T-cell subsets (Tregs), and exhausted CD4 and CD8 cells. (H) Donut plots showing TCR clonotype distribution in TIL products, with black bands indicating the overlap between tumor-resident and expanded T-cell populations. (I) Dot plots comparing TIL expansion across key clonality metrics (TCR count, unique TCR count, D50 Index, diversity index, and entropy).

Figure 2: T-cell receptor (TCR) sequencing of Tumor-Infiltrating Lymphocyte (TIL) and corresponding tumor tissues.
(A) Overlay histogram of TIL+ samples showing the clonal overlap between tumor-resident and expanded TIL populations. Histogram displaying the distribution of TCR clonotypes within the tumor tissue. Each bar represents the frequency of a unique TCR clone within the tumor-resident T-cell population, ranked from most frequent to the least. The vertical red dashed lines indicate shared T-cell clonotypes present in both the tumor tissue and the expanded TIL product. Higher overlap in the more frequent half of the TCR clones suggests that pre-existing tumor-reactive T cells were successfully propagated during expansion (Chi-squared test with Yates' continuity correction). TCRseq of TIL product was not conducted in sample 22-0189 because of limited generation of TIL, hence no matched TCR clone was shown. **(B)**: Histogram of clonal distribution of TIL- tumor tissues. **(C)** Immune Pathway and Cell Type Enrichment: Heatmap of GSVA scores showing key immune pathways in TIL+ tumors (blue) and TIL- (red) tumors. TIL+ tumors exhibit higher Th1 and pro-inflammatory signatures, while TIL- tumors show increased Treg, Th2, and anti-inflammatory pathways. These data provide insight into TIL clonal dynamics and their potential contribution to anti-tumor immunity.

Figure 3. Clinical and MRI Characteristics of eight glioma patients arranged by Tumor-Infiltrating Lymphocyte (TIL) expansion success during *ex vivo* expansion with IL-2. For each patient, axial T2-weighted FLAIR (left) and T1-weighted post-contrast (right) images are presented, highlighting tumor location and imaging features**.**

Figure 4: Immune Composition and Gene Expression Differences Between Tumor-Infiltrating Lymphocyte (TIL) + and – tumors (A–B) Immune Composition Analysis: Stacked bar plots depict the proportional differences in immune subsets between TIL+ and TIL− tumors. TIL+ tumors exhibit a higher presence of cytotoxic CD8+ T cells and pro-inflammatory immune subsets, while TIL− tumors are enriched in

immunosuppressive populations, including Tregs and macrophages. **(C)** Volcano plot of differentially expressed genes between TIL+ and TIL− tumors. Genes upregulated in TIL+ tumors are highlighted in blue, while genes upregulated in TIL− tumors are shown in red. The x-axis represents the log2 fold change, and the y-axis represents the -log10 adjusted p-value. Genes with significant differential expression (adjusted $p < 0.05$) are annotated. **(D)** Volcano lot of differentially expressed genes in TIL+ and TIL− Tumors (Xenium Spatial Transcriptomics). TIL− tumors upregulate genes linked to tumor-intrinsic pathways and immune exclusion. These findings highlight the immune-permissive nature of TIL+ tumors, which contrasts with the immunosuppressive and immune-excluded phenotype of TIL− tumors.

Figure 5: Histological and Spatial Transcriptomic Characterization of Tumor-Infiltrating Lymphocyte (TIL) + and – tumors. H&E-stained sections from TIL+ tumors illustrate tissue architecture and cellular density. Xenium spatial transcriptomic maps show gene expression distribution, while high-resolution Xenium Explorer images highlight lymphoid cells (yellow) near endothelial cells (red), suggesting an immune-permissive microenvironment. Spatial immune clustering, associated with successful TIL expansion, also identifies tumor-connected TAMs (green) localized in necrotic, fibrotic, or liquefied tumor regions. In contrast, TIL− tumors exhibit preserved architecture with sparse immune cell populations. Xenium Explorer images reveal tumor and stromal components of these immunologically “cold” tumors with minimal immune clustering. Scale bars represent 100 µm.

Figure 6: Co-Detection by Indexing (CODEX) analysis of Tumor-Infiltrating Lymphocyte (TIL) + and – tumors. (A) Schematic representation of multiplex staining and imaging workflow. (B) Marker panel includes CD163 (macrophages), CD31 (vasculature), CD8 (cytotoxic T cells), CD38 (activated immune cells), CD45 (leukocytes), CD11b (myeloid cells), B-catenin (tumor cells), and DAPI (nuclei). (C) Glioblastoma samples with successful TIL expansion (TIL+). Insets (right) highlight regions of immune infiltration, showing clustering of CD8+ T cells and other immune subsets. (D) Glioblastoma samples without TIL expansion (TIL-). Insets (right) reveal sparse immune cell presence with limited CD8+ T cell infiltration. (E) Comparison of TIL+ and TIL- samples, illustrating differential immune cell distribution and density. Scale bars represent 100 µm.

Supplementary Tables

Supplementary Table 1; Antibodies used for TIL flow cytometry assays
Supplementary Table 2; Gene signatures for Immunophenotyping analysis
Supplementary Table 3; Differential upregulated and downregulated genes in the single cell RNA sequencing data from Tumor-Infiltrating Lymphocyte (TIL) + and – tumors

Supplementary Table 4; Supplementary Table 3; Differential upregulated and downregulated genes in the Xenium spatial transcriptomics data from Tumor-Infiltrating Lymphocyte (TIL) + and – tumors

Supplementary Table 5; Antibodies used for the Co-Detection by Indexing (CODEX) assays

Supplementary Table 6: Clinical and demographic data for 11 glioma patients (18 TIL expansion attempts). Each column represents a TIL product, identified by unique ID. Rows include patient age, sex, tumor type (glioblastoma or anaplastic astrocytoma), resection status (new or recurrent), IDH status, tumor location, and preREP adjunctive therapies. All samples underwent IL-2–based TIL expansion; select samples also received immune-modulating antibodies (atezolizumab, nivolumab, pembrolizumab, or urelumab).

Supplementary Figures

Supplementary Figure 1:
(A) Flow cytometry of TILs from 20 glioma patients.
(B–C) Comparison of preREP and REP TIL composition in two patients (23-0257, 23-0153).
(D) γδ T cell populations in expanded TILs.

Supplementary Figure 2:
Violin plots comparing TIL^+ vs. TIL^- tumors across clonality metrics (Diversity Index, Entropy, Unique CDR3s, D50). No significant differences observed ($p > 0.05$), though trends in D50 and CDR3 counts suggest potential clonality differences.

Supplementary Figure 3:
UMAP plots of scRNA-seq and spatial data showing distinct cellular compositions between TIL^+ and TIL^- tumors, with variable immune infiltration and TAM profiles across patients.

Supplementary Figure 4:
(A) UMAP shows enrichment of immune cells in TIL^+ tumors and neuronal/OPC cells in TIL^- tumors ($p < 0.03$).
(B) Cell type proportions across groups.
(C) Sample-colored UMAPs highlight inter-patient heterogeneity and clustering biases due to sample variability.

Supplementary Figure 5:
Violin plots of immune and tumor cell populations:
(A) Immune cell distribution in TIL^+/TIL^- tumors.
(B) Tumor cell subtypes (AC-, MES-, NPC-, OPC-like).
(C) TAM states (immunosuppressive vs. pro-inflammatory).
(D) Vascular gene expression in TIL^+ tumors.
(E) Glial/neuronal cell proportions.

Supplementary Figure 6:
Violin plots from Xenium data show:
(A) Lymphoid gene expression,
(B) Tumor-intrinsic immune-regulatory genes,
(C) TAM variations,
(D) Endothelial, neuronal, and oligodendroglial markers. Plot width reflects intratumoral expression heterogeneity.

Supplementary Figure 7; **Tumor-connected TAMs localize to necrotic, liquefied, or fibrotic regions in gliomas.** H&E-stained sections from patient tumors aligned with Xenium spatial segmentation show that green-labeled tumor-connected TAMs are mostly in areas of necrosis (23-0227), liquefactive necrosis with viable tumor interfaces (23-0264, 23-0258), or fibrotic and calcified regions (22-0160), and are less abundant in viable tumor nests. These macrophages express stemness, neural, and glial markers (e.g., SOX2, NES, AQP4), suggesting phagocytosis of tumor cells, reprogramming, or mimicry. Their confinement to degenerating regions and enrichment in TIL^- tumors point to a potential role in immune exclusion and tumor-associated tissue remodeling. Abbreviations; F: Female, M: Male, R: Recurrent Disease, ND: Newly Diagnosed Disease. IDH: Isocitrate Dehydrogenase mutations: AA: Anaplastic Astrocytoma, yo: years old.

Figure 1

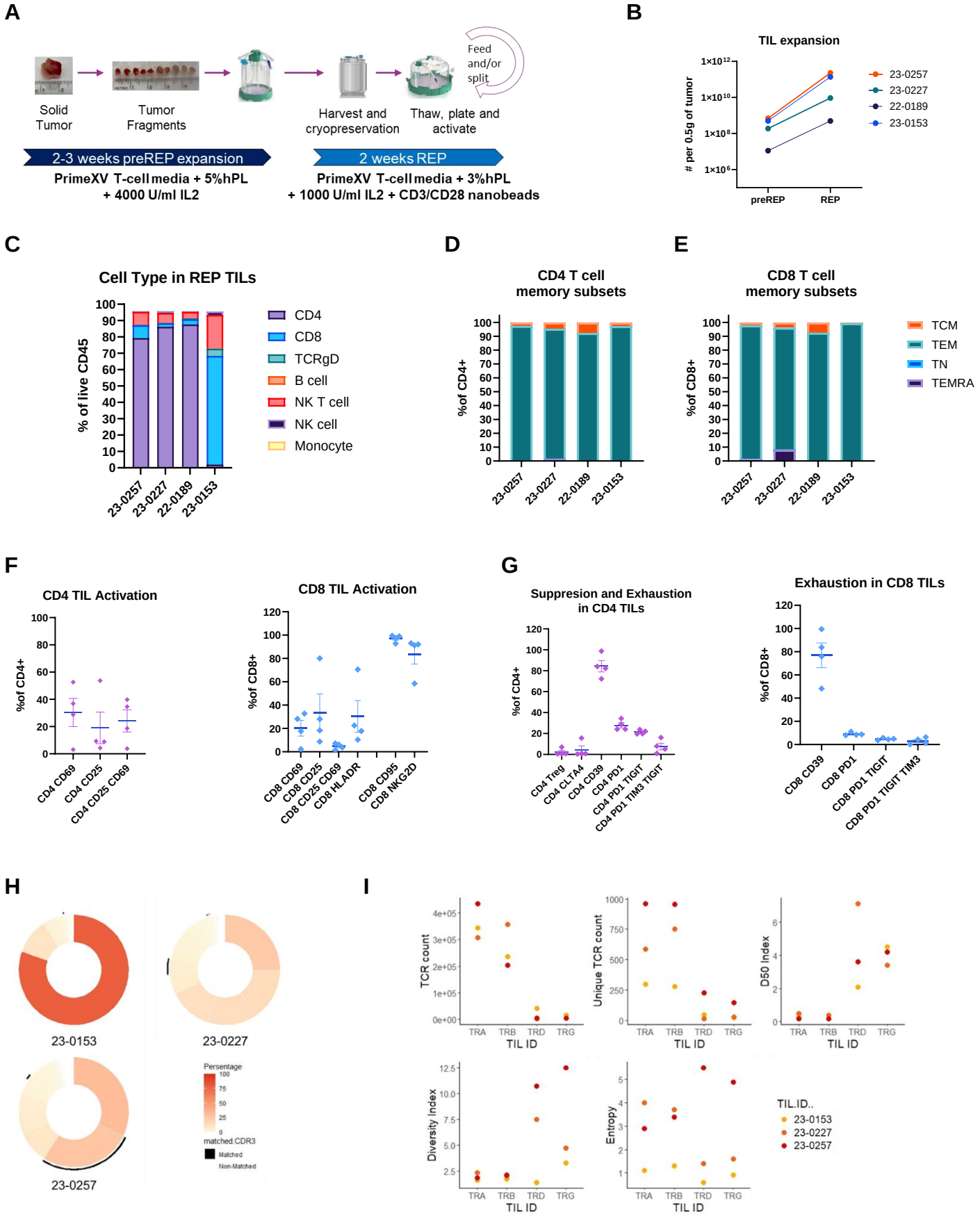
A
Solid Tumor
Tumor Fragments
Harvest and cryopreservation
Thaw, plate and activate
Feed and/or split
2-3 weeks preREP expansion
PrimeXV T-cell media + 5%hPL + 4000 U/ml IL2
2 weeks REP
PrimeXV T-cell media + 3%hPL + 1000 U/ml IL2 + CD3/CD28 nanobeads
B
TIL expansion
per 0.5g of tumor
preREP
REP
23-0257
23-0227
22-0189
23-0153
C
Cell Type in REP TILs
% of live CD45
CD4
CD8
TCRgD
B cell
NK T cell
NK cell
Monocyte
D
CD4 T cell memory subsets
%of CD4+
E
CD8 T cell memory subsets
%of CD8+
TCM
TEM
TN
TEMRA
F
CD4 TIL Activation
CD4 CD69
CD4 CD25
CD4 CD25 CD69
CD8 TIL Activation
CD8 CD69
CD8 CD25
CD8 CD25 CD69
CD8 HLADR
CD8 CD95
CD8 NKG2D
G
Suppresion and Exhaustion in CD4 TILs
CD4 Treg
CD4 CLTA4
CD4 CD39
CD4 PD1
CD4 PD1 TIGIT
CD4 PD1 TIM3 TIGIT
Exhaustion in CD8 TILs
CD8 CD39
CD8 PD1
CD8 PD1 TIGIT
CD8 PD1 TIGIT TIM3
H
23-0153
23-0227
23-0257
Persentage
matched.CDR3
Matched
Non-Matched
I
TCR count
Unique TCR count
D50 Index
Diversity Index
Entropy
TIL ID
TRA
TRB
TRD
TRG
TIL.ID..
23-0153
23-0227
23-0257

Figure 2

(A)

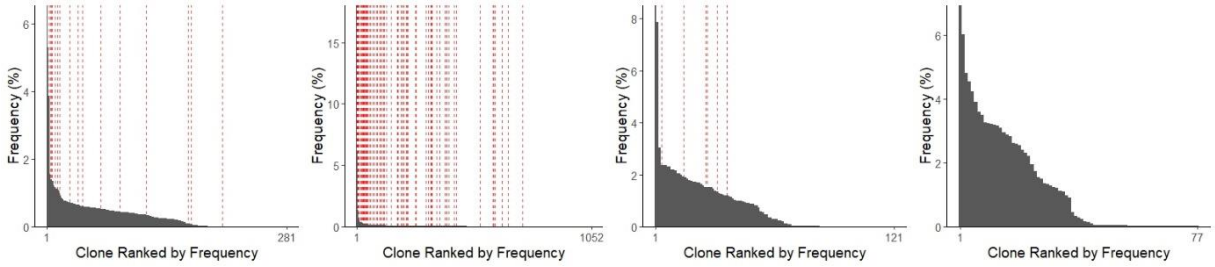

23-0153

	High-frequency Clones	Low-frequency Clones
Matched	13	3
Unmatched	127	136

P value = 0.0213

23-0227

	High-frequency Clones	Low-frequency Clones
Matched	56	13
Unmatched	320	362

P value < 0.0001

23-0257

	High-frequency Clones	Low-frequency Clones
Matched	7	0
Unmatched	472	479

P value = 0.02284

22-0189

(B)

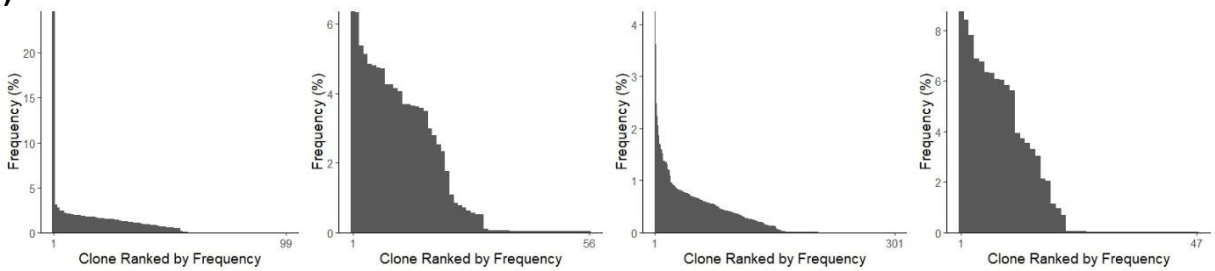

22-0160 **23-0021** **23-0258** **23-0264**

(C)

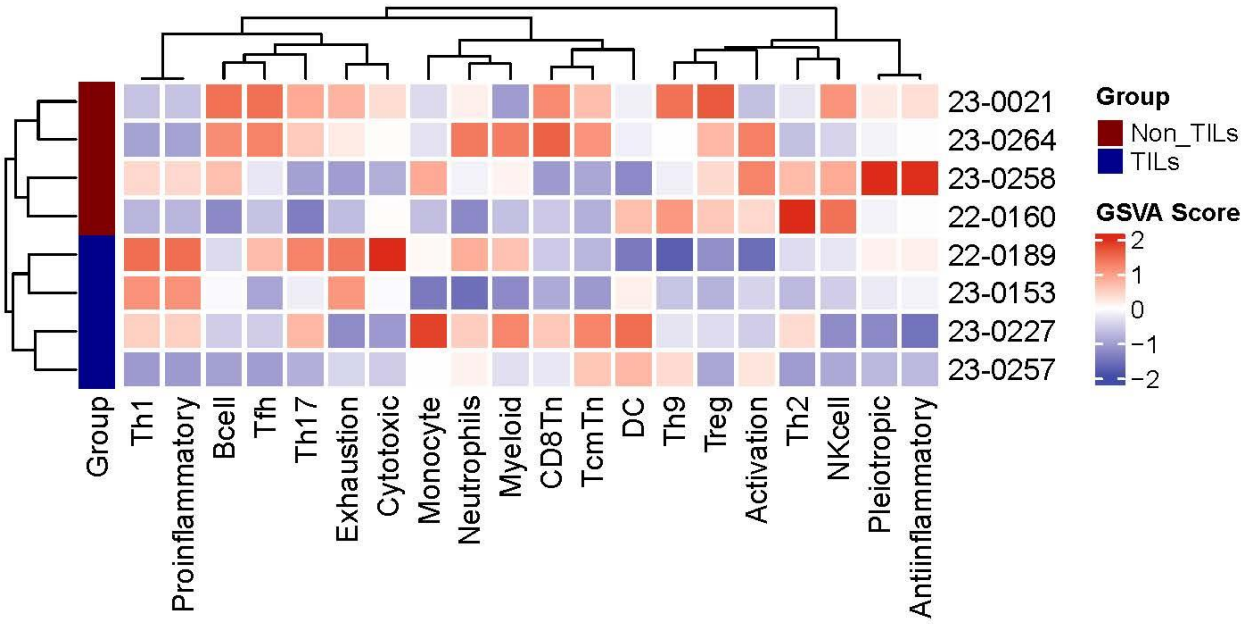

Figure 3

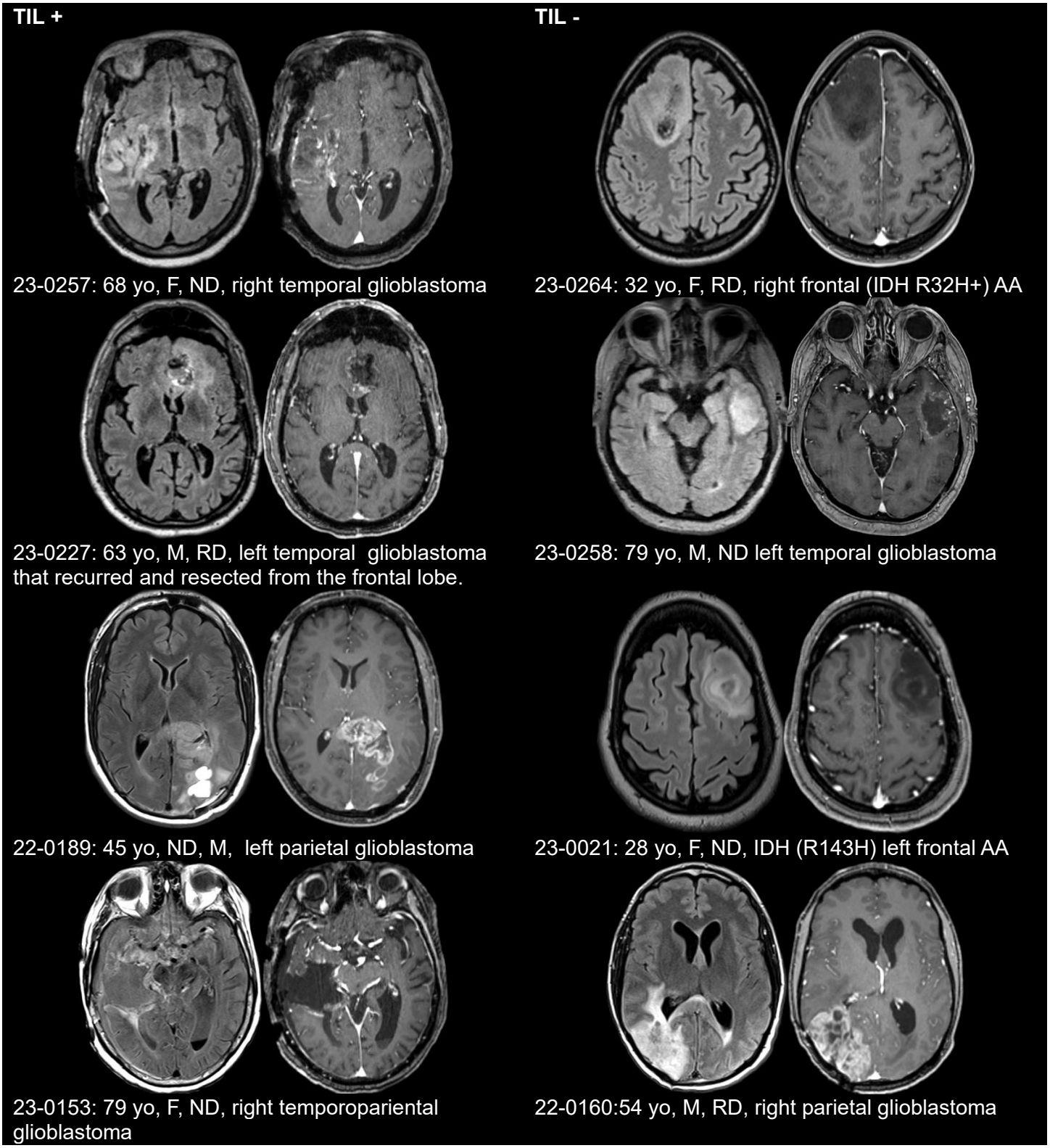

Abbreviations; F: Female, M: Male, R: Recurrent Disease, ND: Newly Diagnosed Disease. IDH: Isocitrate Dehydrogenase mutations: AA: Anaplastic Astrocytoma, yo: years old.

Figure 4

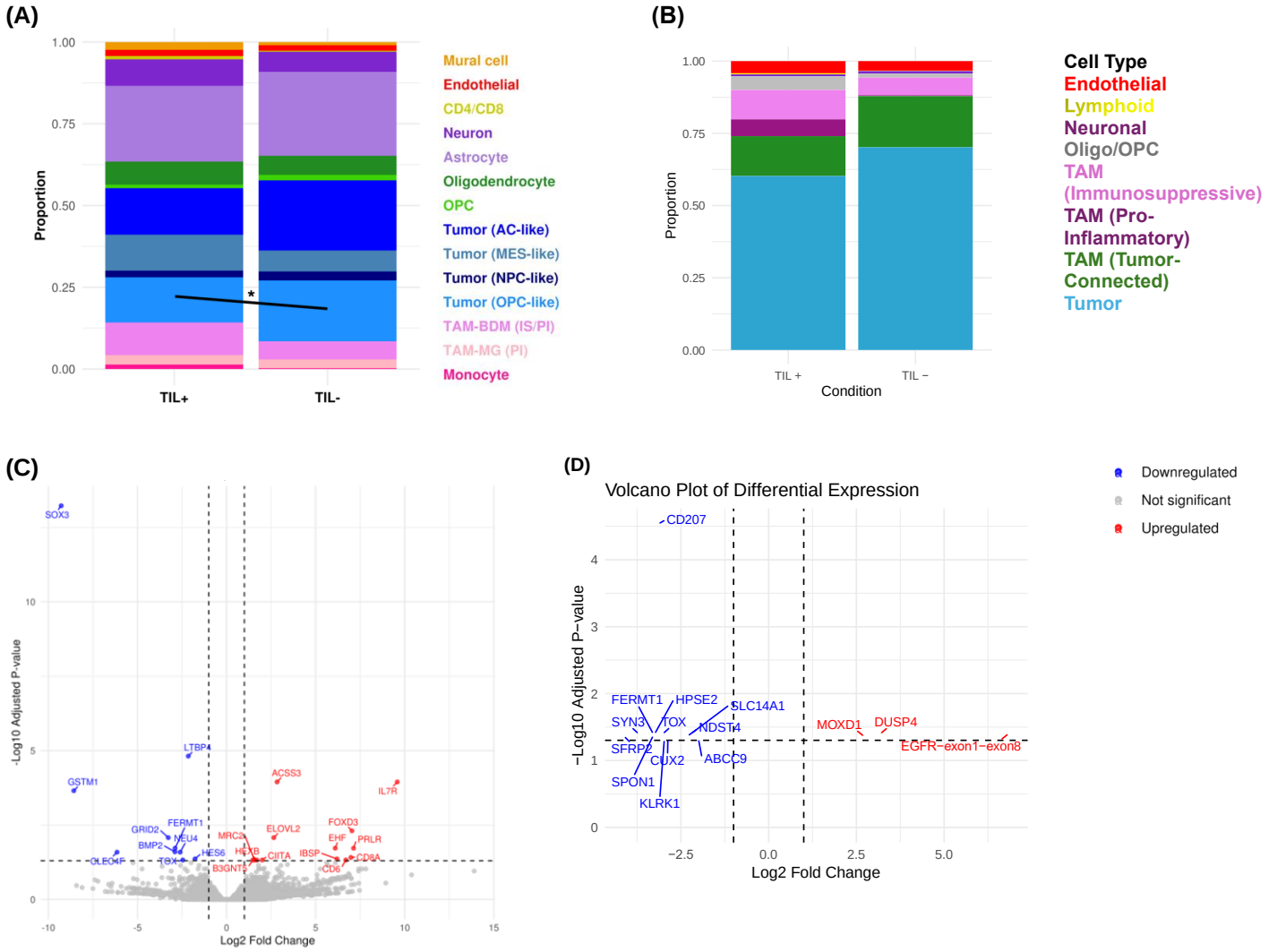
(A)
Proportion
1.00
0.75
0.50
0.25
0.00
TIL+
TIL-
*
Mural cell
Endothelial
CD4/CD8
Neuron
Astrocyte
Oligodendrocyte
OPC
Tumor (AC-like)
Tumor (MES-like)
Tumor (NPC-like)
Tumor (OPC-like)
TAM-BDM (IS/PI)
TAM-MG (PI)
Monocyte
(B)
Proportion
1.00
0.75
0.50
0.25
0.00
TIL +
TIL −
Condition
Cell Type
Endothelial
Lymphoid
Neuronal
Oligo/OPC
TAM (Immunosuppressive)
TAM (Pro-Inflammatory)
TAM (Tumor-Connected)
Tumor
(C)
-Log10 Adjusted P-value
Log2 Fold Change
SOX3
LTBP4
GSTM1
ACSS3
IL7R
GRID2
FERMT1
NEU4
BMP2
MRC2
ELOVL2
FOXD3
EHF
PRLR
OLEO4F
TBX4
HES6
HEXB
CIITA
IBSP
CD8A
B3GNT5
CD6
(D)
Volcano Plot of Differential Expression
Downregulated
Not significant
Upregulated
−Log10 Adjusted P−value
Log2 Fold Change
CD207
FERMT1
HPSE2
SLC14A1
SYN3
TOX
NDST4
SFRP2
CUX2
ABCC9
SPON1
KLRK1
MOXD1
DUSP4
EGFR−exon1−exon8

Figure 5

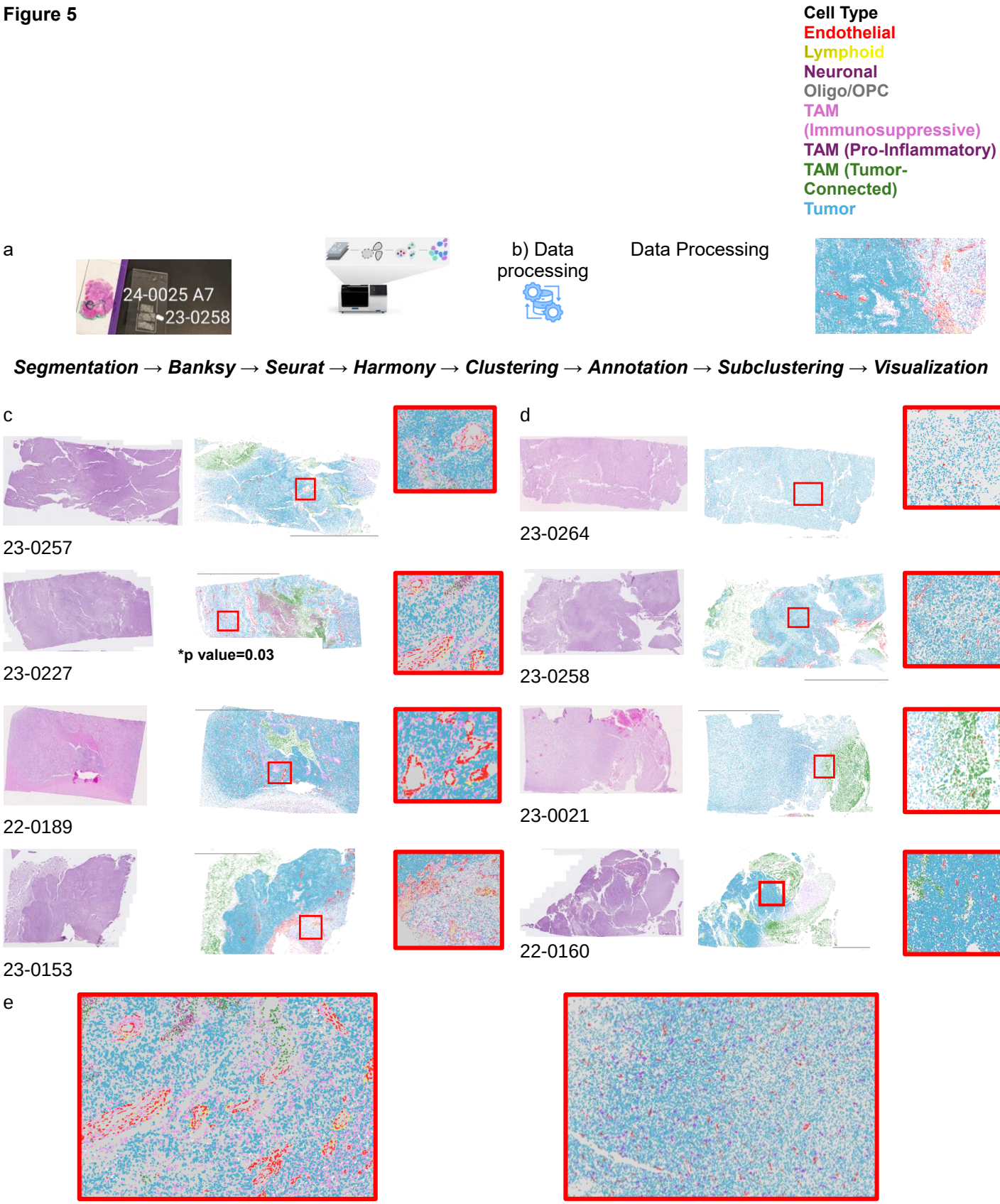
Cell Type
Endothelial
Lymphoid
Neuronal
Oligo/OPC
TAM (Immunosuppressive)
TAM (Pro-Inflammatory)
TAM (Tumor-Connected)
Tumor
a
24-0025 A7
23-0258
b) Data processing
Data Processing
Segmentation → Banksy → Seurat → Harmony → Clustering → Annotation → Subclustering → Visualization
c
23-0257
23-0227
*p value=0.03
22-0189
23-0153
d
23-0264
23-0258
23-0021
22-0160
e

Figure 6

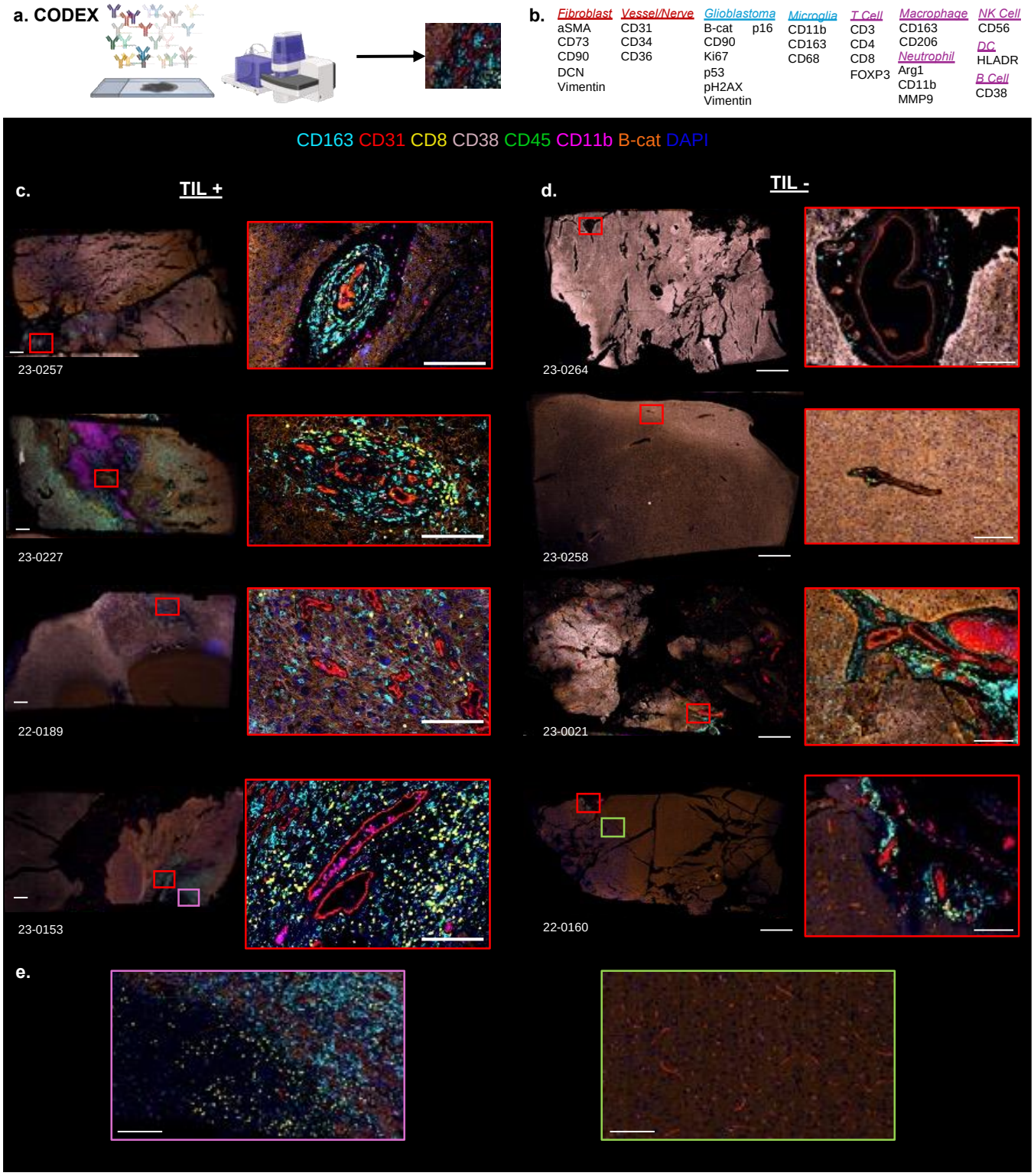
a. CODEX
b.
Fibroblast
aSMA
CD73
CD90
DCN
Vimentin
Vessel/Nerve
CD31
CD34
CD36
Glioblastoma
B-cat
p16
CD90
Ki67
p53
pH2AX
Vimentin
Microglia
CD11b
CD163
CD68
T Cell
CD3
CD4
CD8
FOXP3
Macrophage
CD163
CD206
Neutrophil
Arg1
CD11b
MMP9
NK Cell
CD56
DC
HLADR
B Cell
CD38
CD163 CD31 CD8 CD38 CD45 CD11b B-cat DAPI
c.
TIL +
d.
TIL -
23-0257
23-0264
23-0227
23-0258
22-0189
23-0021
23-0153
22-0160
e.

Supplementary material

Supplementary Table 1

color	marker	clone	catalog #	vendor
BUV395	CD25	BC96	567483	BD
Live/Dead Blue	Live/dead			invitrogen
BUV496	CD28	CD28.2	741168	BD
BUV563	Lag3	3DS223H	365-2239-42	invitrogen
BUV615	CD4	SK3	612987	BD
BUV661	CD19	HIB19	741604	BD
BUV737	CD69	FN50	612818	BD
BUV805	CD3e	UCHT1	612896	BD
BV421	TCR γδ	11F2	744870	BD
BV480	PD1	EH12.1	566112	BD
BV510	HLA-DR	L243	307646	biolegend
BV605	CD57	NK-1	567205	BD
BV650	CD56	NCAM16.2	564057	BD
BV711	CD103	Ber-ACT8	563162	BD
BV750	CD127	HIL-7R-M21	747089	BD
BV785	TIM3	F38-2E2	345032	biolegend
FITC	TCR γδ2	B6	331406	biolegend
Spark Blue 574	CD8	sk1	344784	biolegend
RB613	PDL1	MIH1	759043	BD
PerCP	CD14	M5e2	301848	biolegend
BB700	TIGIT	741182	747846	BD
RB744	NKG2D	1D11	758092	BD
RB780	CXCR6	13B1E5	755573	BD
PE	Foxp3	PCH101	12-4776-42	invitrogen
PE-CF594	CD45RA	HI100	562298	BD
PE-Cy5	CD39	A1	328248	biolegend
PE-Fire 700	CD95	DX2	305666	biolegend
PE-Cy7	TCR γδ1	T28.2	25-5679-42	invitrogen
PE-Fire 810	CTLA4	BNI3	369639	biolegend
APC	CD137	4B4-1	550890	BD
APC-R700	CD45	HI30	566041	BD
APC-Cy7	CCR7	G043H7	353212	biolegend

Supplementary Table 2

Term	Gene signature
Th1	IFNG, TBX21, CCL5, CXCR3, TBX21, STAT11
Th2	IL4, IL5, IL13, GATA3, STAT6, IL1RL1
Th9	IL9, IL10, SPI1, STAT5A
Th17	IL23R, RORC, STAT3
Tfh	BCL6, ICOS, CXCR5, IL21, CD38
Treg	FOXP3, IKZF2, IL10, LAG3, TGFB1, IL2RA, STAT5A
CD8Tn	CD8A, CD8B, LAG3, TCF7, SELL
TcmTn	CCR7, CD8A, SELL
Exhaustion	PDCD1, CTLA4, LAG3, HAVCR2, TIGIT, IDO1, PVR
Bcell	TNFRSF17, BTK, CD19, CD22, CD40, CD79A, CD79B, CXCR5, FCGR2B, BCL6, CD38, CD27, CD5
NKcell	KLRD1, KLRB1, KLRC1, NCR2, NCR3, KLRC1, SLAMF7, FCGR3A
Myeloid	MPO, CD14, CD68, ITGAM
Monocyte	ITGAM, CD14, FCGR3A, FCGR2A, FCGR1A, CD68, MRC1, FCGR2B, MPO, S100A8, PADI4
DC	ITGAX, CD40, CD83, IL3RA, HLA-DRA, ITGAE, S100A9
Eosinophils	EPX, IL5, IL4, IL13
Neutrophils	MPO, PADI4, CD14, FCGR3A
Pro-inflammatory	CCL5, IFNG, IL9, IL12B, IL13, IL21, TNF
Anti-inflammatory	IL10, IL4, IL1R1, IL5
Pleiotropic	IL5, IL21, IL23A, IL27
Activation	TNFRSF9, IL2RA, CD38, CD63, CD69, CD226, CXCR3, ICOS, KLRB1, KLRD1, TFRC
Cytotoxic	GZMB, PRF1, FAS, IFNG

Supplementary Table 3

Upregulated Genes in TIL+ group				
Gene	**log2FC**	**p-value**	**adj. p-value**	**Status**
IL7R	9.58	2.47E-08	1.13E-04	upReg
ACSS3	2.83	2.88E-08	1.13E-04	upReg
FOXD3	7.04	1.90E-05	1.90E-02	upReg
ELOVL2	7.13	1.92E-05	1.90E-02	upReg
PRLR	6.96	3.89E-05	3.89E-02	upReg
EHF	6.94	3.98E-05	3.98E-02	upReg
CD8A	6.97	4.74E-05	4.74E-02	upReg
IBSP	1.56	4.74E-05	4.74E-02	upReg
MRC2	1.56	4.74E-05	4.74E-02	upReg
B3GNT3	1.69	4.74E-05	4.74E-02	upReg
CIITA	1.69	4.74E-05	4.74E-02	upReg
HEXB	1.69	4.74E-05	4.74E-02	upReg
CD6	1.69	4.74E-05	4.74E-02	upReg
HOXC13	5.62	9.33E-05	5.86E-02	nonDE
IL18R1	6.11	9.35E-05	5.86E-02	nonDE

Upregulated Genes in TIL- group				
Gene	**log2FC**	**p-value**	**adj. p-value**	**Status**
SOX3	9.28	5.88E-14	1.13E-04	upReg
LTBP4	2.15	1.96E-09	1.13E-04	upReg
GSTM1	2.89	7.11E-08	4.96E-03	upReg
GRID2	2.74	4.06E-06	8.40E-03	upReg
FERMT1	2.68	1.33E-05	1.90E-02	upReg
BMP2	2.65	1.19E-05	1.90E-02	upReg
CLEC4F	2.65	2.22E-05	3.89E-02	upReg
NEU4	2.27	2.31E-05	4.35E-02	upReg
HES6	1.77	4.64E-05	4.74E-02	upReg
TOX	1.74	5.90E-05	4.74E-02	upReg
CD207	1.58	1.01E-04	5.86E-02	nonDE
SOX8	1.52	1.01E-04	5.86E-02	nonDE
ZFPM2	1.36	1.59E-04	7.24E-02	nonDE
PTCH1	1.52	1.48E-04	7.24E-02	nonDE
RTP5	1.32	1.69E-04	7.78E-02	nonDE

Supplementary Table 4

logFC	FDR	gene	significant
6.8331692	0.0398152	*EGFR-exon1-exon8*	Upregulated
3.1837521	0.0398152	*DUSP4*	Upregulated
2.7139088	0.0435637	*MOXD1*	Upregulated
-2.00053	0.0483727	*ABCC9*	Downregulated
-2.217396	0.0398152	*SLC14A1*	Downregulated
-2.304604	0.0427589	*NDST4*	Downregulated
-2.875229	0.0483727	*CUX2*	Downregulated
-2.975365	0.0494847	*KLRK1*	Downregulated
-3.00894	0.0398152	*TOX*	Downregulated
-3.138759	0.000029	*CD207*	Downregulated
-3.244759	0.0398152	*HPSE2*	Downregulated
-3.29303	0.0398152	*FERMT1*	Downregulated
-3.293543	0.0427589	*SPON1*	Downregulated
-3.711017	0.0398152	*SYN3*	Downregulated
-4.115114	0.0435637	*SFRP2*	Downregulated
3.7625388	0.2611661	*TRDC*	Not significant
3.4810509	0.1393094	*CXCL8*	Not significant
2.7200506	0.1887431	*LHX6*	Not significant
2.6953447	0.0589641	*NPY*	Not significant

Supplementary Table 5

Antibody	Clone	Company	Catalog Number	Oligo
Arg1	Polyclonal			43
aSMA	Polyclonal	abcam	AB5694	69
B-cat	14	CellMarque		51
BCL2	124	CellMarque		41
CD11b	EPR1344	abcam	ab209970	28
CD138	DL-101	Biolegend	352302	76
CD163	EDHu-1	Novus	NB100-64980	45
CD20	rIGEL/773	Noovus	NBP2-54591	48
CD206	E2L9N	CST	49243SF	55
CD25	4C9	CellMarque	custom	24
CD3	MRQ-39	CellMarque	MRQ-39	77
CD31	C31.3+C31.7+C31.10	Novus	NBP2-47785	68
CD34	QBEnd/10			38
CD36	D8L9T			74
CD38	E7Z8	CST		66
CD4	EPR6855	abcam	ab181724	20
CD45	2B11 + PD7/26	Novus	NBP2-34287	56
CD56	MRQ-42	CellMarque	custom	29
CD68				
CD73	Polyclonal	BD	AF5795	75
CD8	C8/144B	Invitrogen	MA5-13473	8
CD90	EPR3132			21
DCN	Polyclonal	Thermo		63
FOXP3	236A/E7	Invitrogen	14-4777-82	61
HLADR	EPR3692	abcam	ab209968	62
Ki67	B56	BD	556003	6
MMP9	L51/82	Biolegend	819701	80
p16	G175-405			59
p53	D07			52
pH2AX	EP854(2)Y			57
Vimentin	RV202	Novus	NBP1-97672	7

Supplementary Table 6

TIL	1	2	3	4	5	6	7	8	9	10	11	12	13	14	15	16	17	18
Tumor																		
Age	68	68	68	68	63	45	79	79	45	45	46	46	46	45	45	75	63	45
Sex																		
Histology																		
Resection																		
IDH																		
Location																		
Adjuncts																		
REP vs. pre-REP																		

Color Key

Tumor samples:

23-0257	23-0227	22-0189	23-0153	23-0059	
23-0196	23-0217	21-0213	21-0221	21-0241	22-0155

Sex: Male Female

Histology: Glioblastoma Anaplastic Astrocytoma

Indication for tumor resection: Newly Diagnosed OR Recurrent Tumor

Isocitrate Dehydrogenase status: (IDH) Wild Type; IDH-Mutated

Tumor Anatomical Location: Frontal Temporal Parietal Midline Occipital

Expansion Protocol: preREP or REP

Adjuncts added to Pre-Rapid Expansion Culture:

IL2 alone Pembrolizumab Nivolumab Atezolizumab Urelumab

Supplementary Figures

Supplementary Figure 1

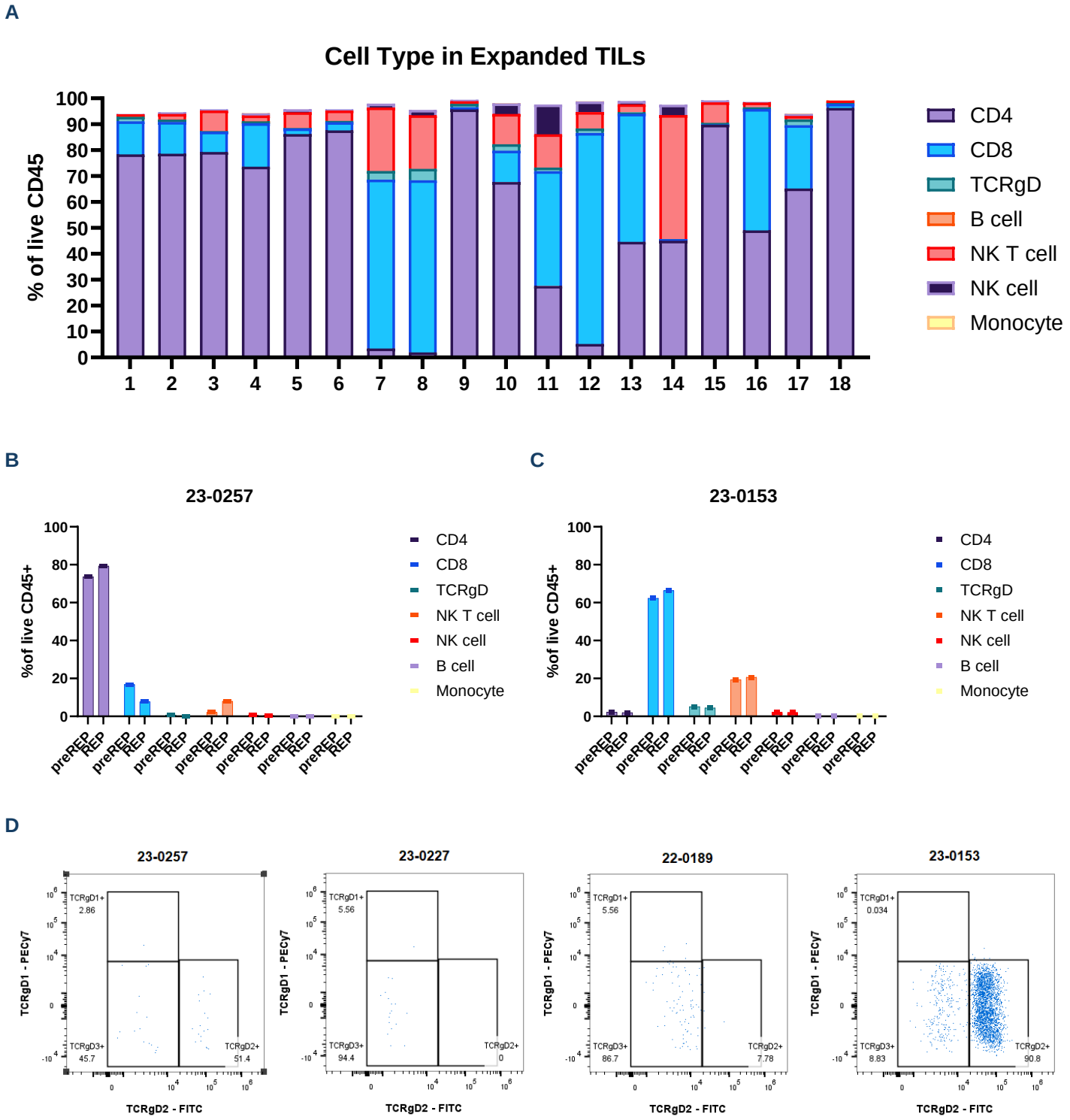

Supplementary Figure 2

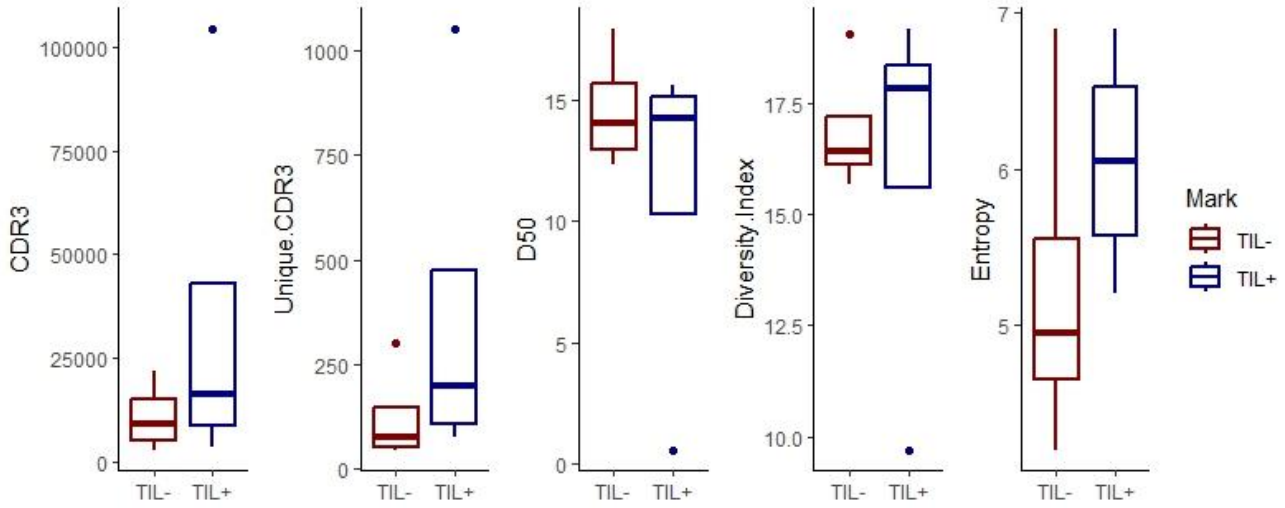

Supplementary Figure 3

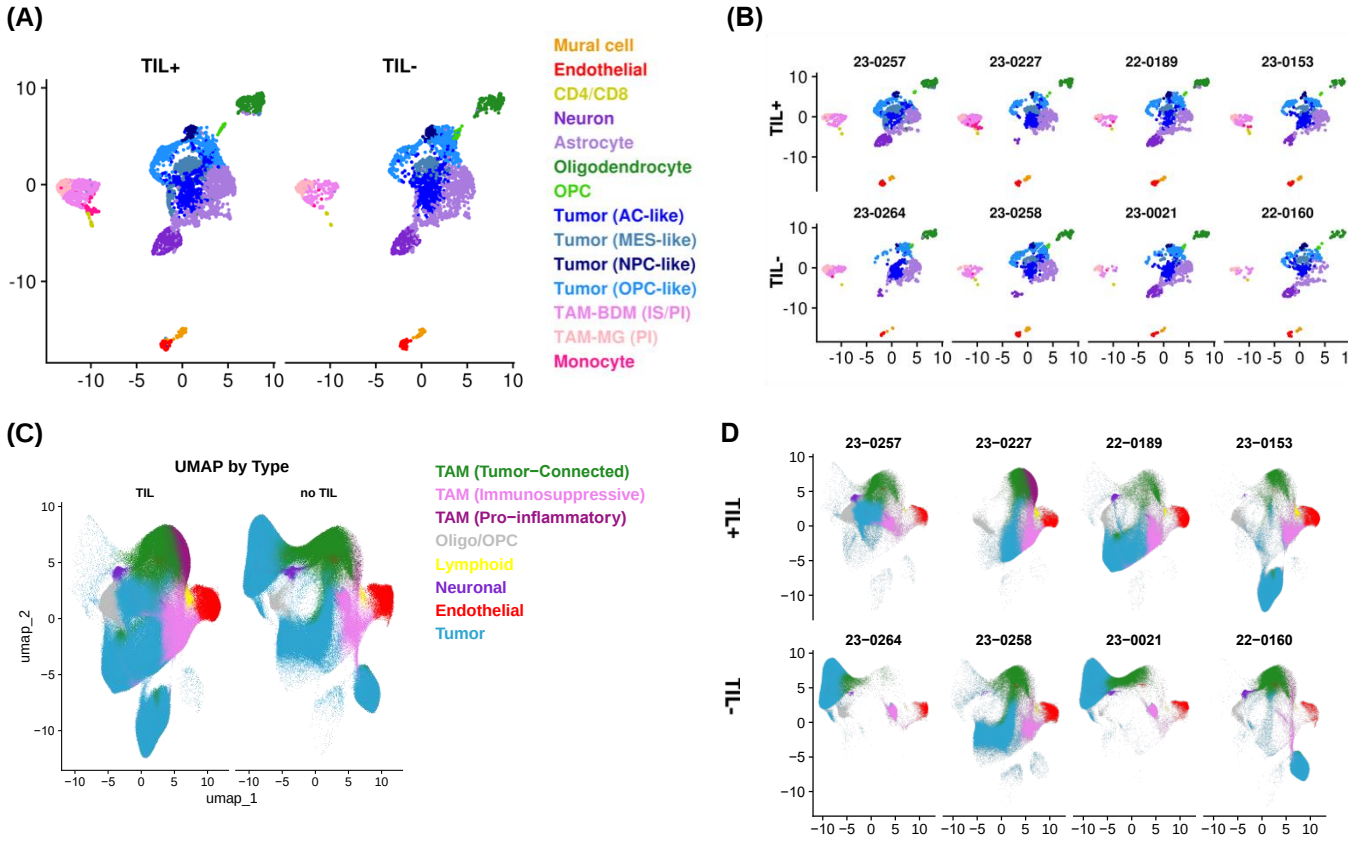

Supplementary Figure 4

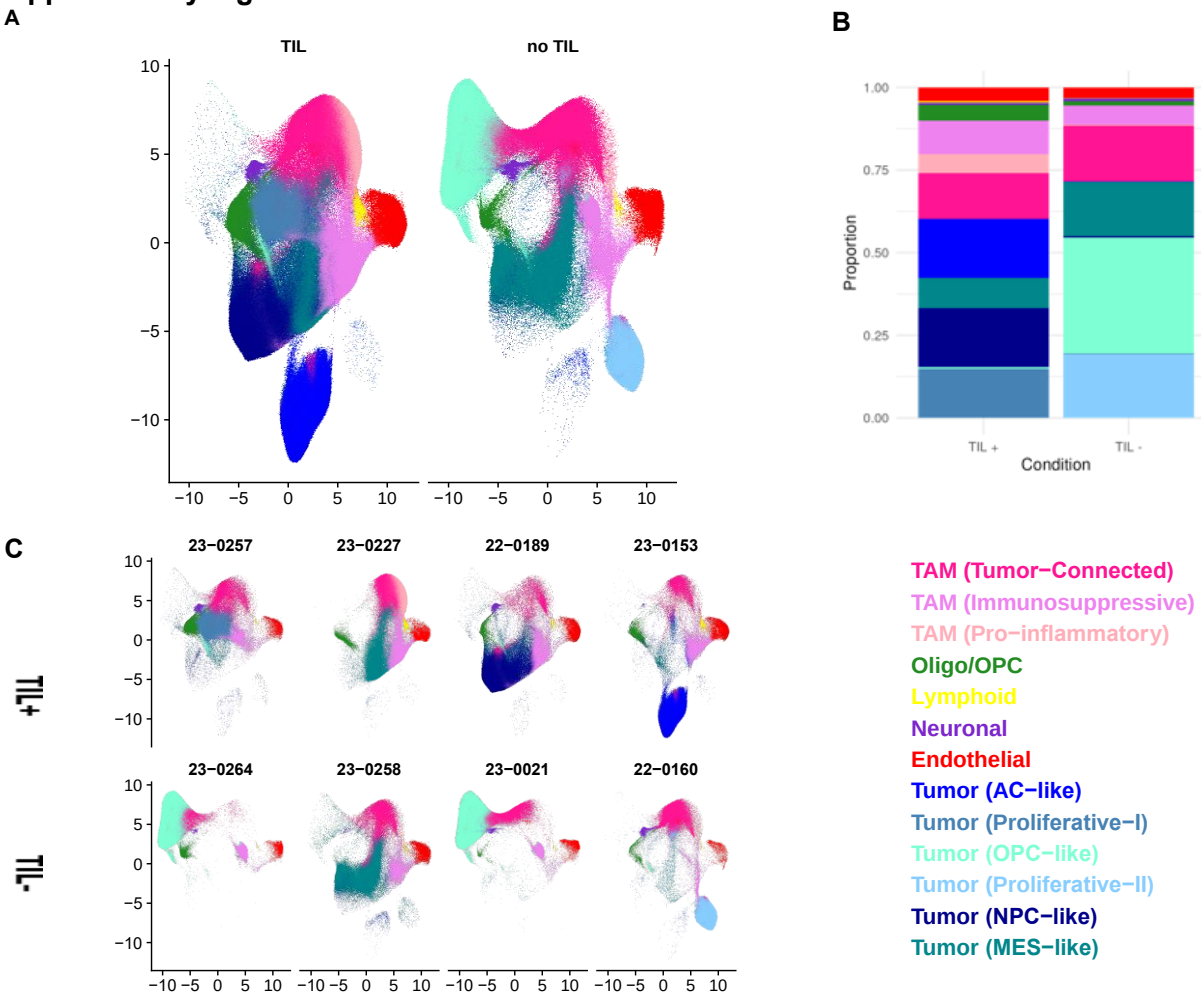

Supplementary Figure 5

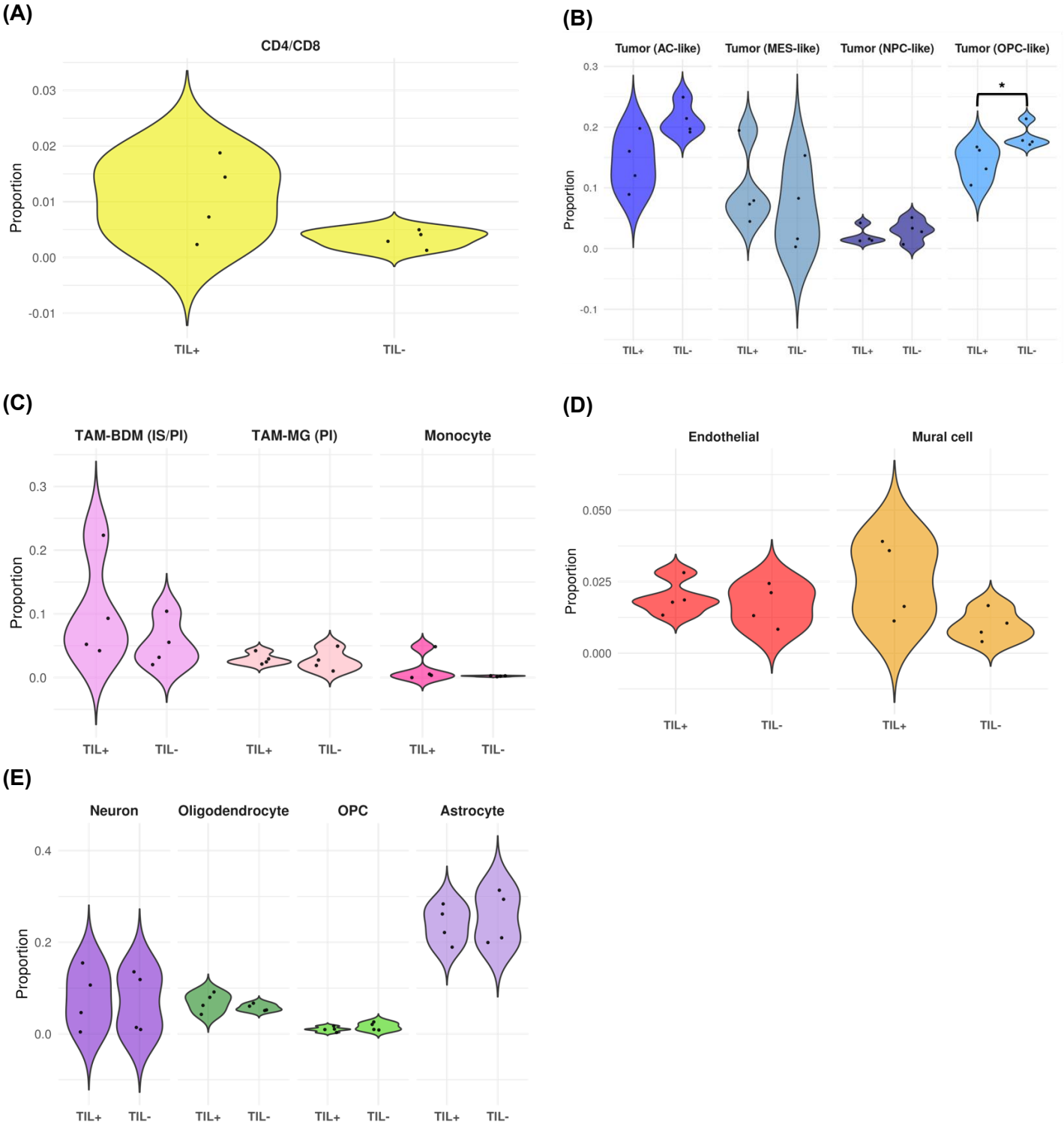

Supplementary Figure 6

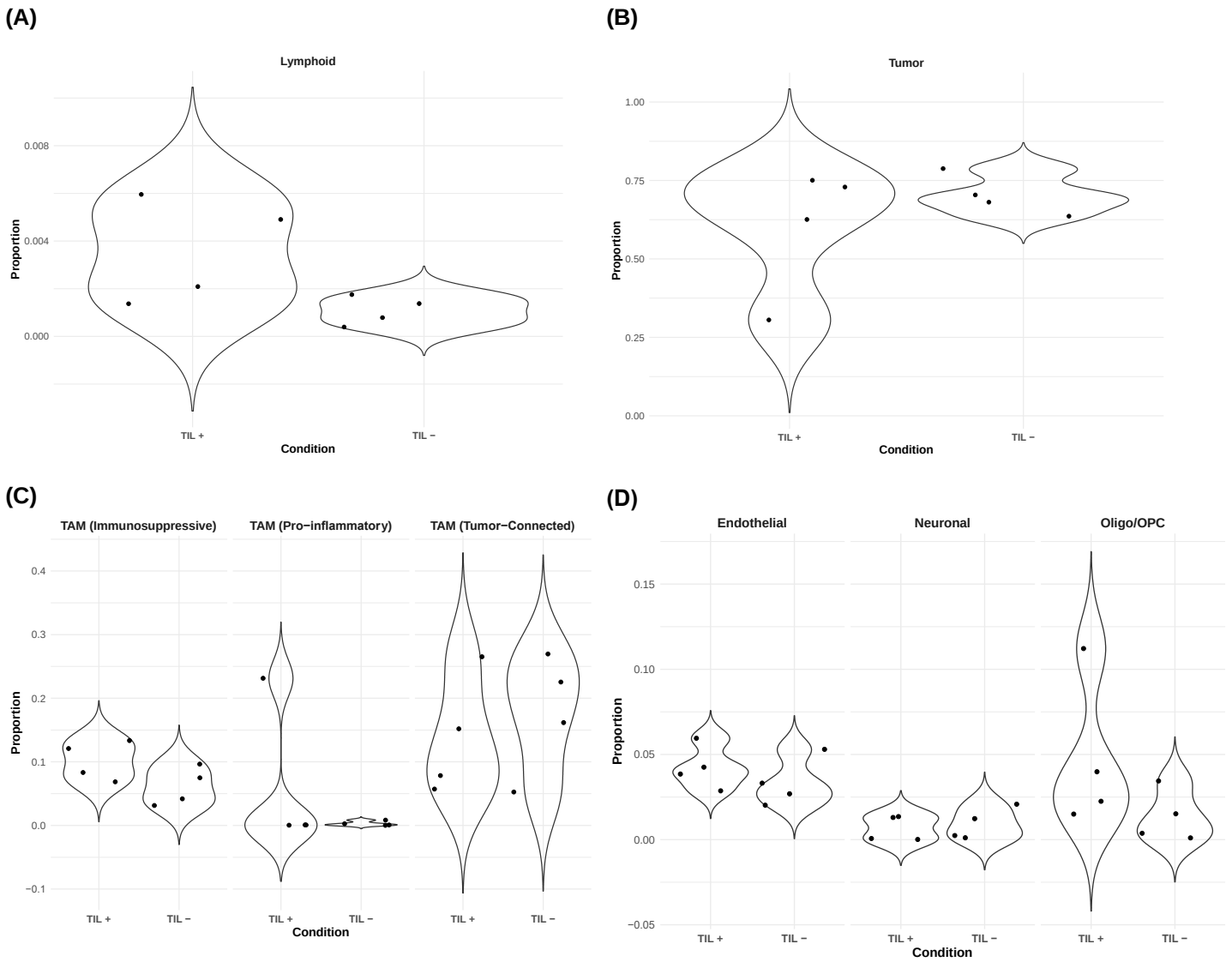

Supplementary Figure 7

23-0257: 68 yo, F, ND, right temporal glioblastoma

Infiltrating tumor periphery exhibiting necrosis with a vacuolated appearance most obvious in upper left corner. Lower part of the box exhibit moderately hypercellular brain tissue with a mix of tumor cells and macrophages.

23-0264: 32 yo, F, RD, right frontal (IDH R32H+) AA

A pale, vacuolated area suggestive of edematous tumor, adjacent to eosinophilic and cellular tissue consistent with viable tumor.

23-0227: 63 yo, M, RD, left temporal glioblastoma that recurred and resected from the frontal lobe.

Necrosis with surrounding viable tumor. The upper half of the boxed region shows viable, densely cellular tumor, whereas the lower half consists of pale necrotic tissue, bordered by a dense cellular rim, indicating a transition to pseudopalisading necrosis.

23-0258: 79 yo, M, ND left temporal glioblastoma

The boxed region shows interface between pale, necrotic or edematous tissue, likely representing necrosis, and adjacent viable, more cellular tumor or stromal tissue in the right side of the box.

22-0189: 45 yo, ND, M, left parietal glioblastoma

A central zone of necrosis with eosinophilic cellular debris, surrounded by pseudopalisading hyperchromatic tumor cells and areas of microvascular proliferation and hemorrhage, characteristic of glioblastoma.

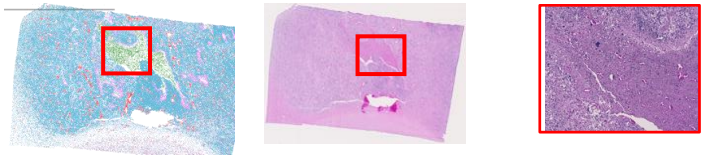

23-0021: 28 yo, F, ND, IDH (R143H) left frontal AA

Infiltrating periphery, transition from viable tumor to a necrotic core, consistent with a pseudopalisading pattern characteristic of high-grade glioma.

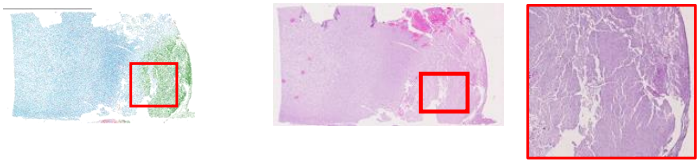

23-0153: 79 yo, F, ND, right temporopariental glioblastoma

Transition from loosely structured, necrotic or edematous tissue on the left to more densely cellular, viable tumor tissue on the right, consistent with a necrosis-viable interface.

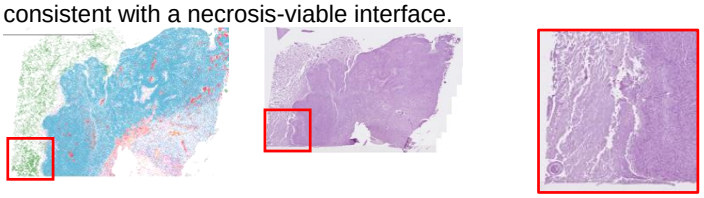

22-0160:54 yo, M, RD, right parietal glioblastoma

Fibrosis with calcification, which is an uncommon unspecific reaction after therapy including post-chemoradiation.

Cell Type
Endothelial
Lymphoid
Neuronal
Oligo/OPC
TAM (Immunosuppressive)
TAM (Pro-Inflammatory)
TAM (Tumor-Connected)
Tumor

References:

1. Rohaan, M.W. *et al.* Tumor-Infiltrating Lymphocyte Therapy or Ipilimumab in Advanced Melanoma. *New England Journal of Medicine* **387**, 2113-2125 (2022).
2. Sarnaik, A.A. *et al.* Lifileucel, a Tumor-Infiltrating Lymphocyte Therapy, in Metastatic Melanoma. *J Clin Oncol* **39**, 2656-2666 (2021).
3. Creelan, B.C. *et al.* Tumor-infiltrating lymphocyte treatment for anti-PD-1-resistant metastatic lung cancer: a phase 1 trial. *Nature medicine* **27**, 1410-1418 (2021).
4. Poschke, I.C. *et al.* The Outcome of Ex Vivo TIL Expansion Is Highly Influenced by Spatial Heterogeneity of the Tumor T-Cell Repertoire and Differences in Intrinsic In Vitro Growth Capacity between T-Cell Clones. *Clin Cancer Res* **26**, 4289-4301 (2020).
5. Chiffelle, J. *et al.* Tumor-reactive T cell clonotype dynamics underlying clinical response to TIL therapy in melanoma. *Immunity* **57**, 2466-2482.e12 (2024).
6. Hickey, J.W. *et al.* Spatial mapping of protein composition and tissue organization: a primer for multiplexed antibody-based imaging. *Nature Methods* **19**, 284-295 (2022).
7. Bressan, D., Battistoni, G. & Hannon, G.J. The dawn of spatial omics. *Science* **381**, eabq4964 (2023).
8. Liu, L. *et al.* Spatiotemporal omics for biology and medicine. *Cell* **187**, 4488-4519 (2024).
9. Chen, J., Larsson, L., Swarbrick, A. & Lundeberg, J. Spatial landscapes of cancers: insights and opportunities. *Nature Reviews Clinical Oncology* **21**, 660-674 (2024).
10. Matusiak, M. *et al.* Spatially Segregated Macrophage Populations Predict Distinct Outcomes in Colon Cancer. *Cancer Discovery* **14**, 1418-1439 (2024).
11. Hickey, J.W. *et al.* T cell-mediated curation and restructuring of tumor tissue coordinates an effective immune response. *Cell Reports* **42**, 113494 (2023).
12. Strasser, M.K. *et al.* Concerted epithelial and stromal changes during progression of Barrett's Esophagus to invasive adenocarcinoma exposed by multi-scale, multi-omics analysis. *bioRxiv*, 2023.06.08.544265 (2023).
13. Baertsch, M.-A., Nolan, G.P. & Hickey, J.W. Multicellular modules as clinical diagnostic and therapeutic targets. *Trends in Cancer* **8**, 164-173 (2022).
14. Hickey, J.W. *et al.* Integrating multiplexed imaging and multiscale modeling identifies tumor phenotype conversion as a critical component of therapeutic T cell efficacy. *Cell Systems* **15**, 322-338.e5 (2024).
15. Hickey, J.W. *et al.* Organization of the human intestine at single-cell resolution. *Nature* **619**, 572-584 (2023).
16. Yang, S., Archer, G.E., Flores, C.E., Mitchell, D.A. & Sampson, J.H. A cytokine cocktail directly modulates the phenotype of DC-enriched anti-tumor T cells to convey potent anti-tumor activities in a murine model. *Cancer immunology, immunotherapy : CII* **62**, 1649-1662 (2013).
17. Ross, S.H. & Cantrell, D.A. Signaling and Function of Interleukin-2 in T Lymphocytes. *Annu Rev Immunol* **36**, 411-433 (2018).
18. Chen, D., Tang, T.X., Deng, H., Yang, X.P. & Tang, Z.H. Interleukin-7 Biology and Its Effects on Immune Cells: Mediator of Generation, Differentiation, Survival, and Homeostasis. *Front Immunol* **12**, 747324 (2021).
19. ElKassar, N. & Gress, R.E. An overview of IL-7 biology and its use in immunotherapy. *J Immunotoxicol* **7**, 1-7 (2010).
20. Pang, N. *et al.* IL-7 and CCL19-secreting CAR-T cell therapy for tumors with positive glypican-3 or mesothelin. *J Hematol Oncol* **14**, 118 (2021).
21. Guertin, D.A. & Wellen, K.E. Acetyl-CoA metabolism in cancer. *Nature Reviews Cancer* **23**, 156-172 (2023).
22. Shi, P. *et al.* MOXD1 knockdown suppresses the proliferation and tumor growth of glioblastoma cells via ER stress-inducing apoptosis. *Cell Death Discovery* **8**, 174 (2022).
23. Paumelle, R. *et al.* Sequential activation of ERK and repression of JNK by scatter factor/hepatocyte growth factor in madin-darby canine kidney epithelial cells. *Molecular biology of the cell* **11**, 3751-3763 (2000).

24. Lin, H., Qiu, S., Xie, L., Liu, C. & Sun, S. Nimbolide suppresses non-small cell lung cancer cell invasion and migration via manipulation of DUSP4 expression and ERK1/2 signaling. *Biomedicine & Pharmacotherapy* **92**, 340-346 (2017).
25. Liu, C. *et al.* FERMT1 mediates epithelial–mesenchymal transition to promote colon cancer metastasis via modulation of β-catenin transcriptional activity. *Oncogene* **36**, 1779-1792 (2017).
26. Sin, S. *et al.* Role of the focal adhesion protein kindlin-1 in breast cancer growth and lung metastasis. *Journal of the National Cancer Institute* **103**, 1323-1337 (2011).
27. Pan, Z. *et al.* FERMT1 suppression induces anti-tumor effects and reduces stemness in glioma cancer cells. *Journal of Cancer Research and Clinical Oncology* **150**, 338 (2024).
28. Bejarano, L. *et al.* Single-cell atlas of endothelial and mural cells across primary and metastatic brain tumors. *Immunity*.
29. Moffet, J.J.D. *et al.* Spatial architecture of high-grade glioma reveals tumor heterogeneity within distinct domains. *Neuro-Oncology Advances* **5**(2023).
30. Ravi, V.M. *et al.* Spatially resolved multi-omics deciphers bidirectional tumor-host interdependence in glioblastoma. *Cancer Cell* **40**, 639-655.e13 (2022).
31. Liu, M. *et al.* Spatial transcriptomics reveals segregation of tumor cell states in glioblastoma and marked immunosuppression within the perinecrotic niche. *Acta Neuropathologica Communications* **12**, 64 (2024).
32. van Hooren, L. *et al.* Agonistic CD40 therapy induces tertiary lymphoid structures but impairs responses to checkpoint blockade in glioma. *Nat Commun* **12**, 4127 (2021).
33. Shen, S. *et al.* Toll-like receptor agonists promote the formation of tertiary lymphoid structure and improve anti-glioma immunity. *Neuro-Oncology* **27**, 140-154 (2024).
34. Vanhersecke, L. *et al.* Standardized Pathology Screening of Mature Tertiary Lymphoid Structures in Cancers. *Laboratory Investigation* **103**, 100063 (2023).
35. Zheng, Y., Carrillo-Perez, F., Pizurica, M., Heiland, D.H. & Gevaert, O. Spatial cellular architecture predicts prognosis in glioblastoma. *Nature Communications* **14**, 4122 (2023).
36. Liu, Y. *et al.* Integration analysis of single-cell and spatial transcriptomics reveal the cellular heterogeneity landscape in glioblastoma and establish a polygenic risk model. *Frontiers in Oncology* **13**(2023).
37. Neftel, C. *et al.* An Integrative Model of Cellular States, Plasticity, and Genetics for Glioblastoma. *Cell* **178**, 835-849.e21 (2019).
38. Hu, C. *et al.* CellMarker 2.0: an updated database of manually curated cell markers in human/mouse and web tools based on scRNA-seq data. *Nucleic Acids Research* **51**, D870-D876 (2022).
39. Farmen, K. *et al.* Monocyte markers correlate with immune and neuronal brain changes in REM sleep behavior disorder. *Proc Natl Acad Sci U S A* **118**(2021).
40. Chen, Y. *et al.* Tumor-associated monocytes promote mesenchymal transformation through EGFR signaling in glioma. *Cell Rep Med* **4**, 101177 (2023).
41. Robinson, M.D., McCarthy, D.J. & Smyth, G.K. edgeR: a Bioconductor package for differential expression analysis of digital gene expression data. *Bioinformatics* **26**, 139-140 (2009).
42. Black, S. *et al.* CODEX multiplexed tissue imaging with DNA-conjugated antibodies. *Nature Protocols* **16**, 3802-3835 (2021).